JOURNAL OF SPACECRAFT AND ROCKETS
Vol. 47, No. 1, January–February 2010

Drag Reduction Using Aerodisks for Hypersonic Hemispherical Bodies

M. Y. M. Ahmed* and N. Qin†
University of Sheffield, Sheffield S1 3JD, England, United Kingdom

DOI: 10.2514/1.46655

The main challenge facing the designers of hypersonic vehicles is the significantly high levels of pressure drag and aerodynamic heating. Although blunt noses are preferred for better heat distribution, they introduce substantial drag to the vehicle. Spikes and aerodisks proved to be efficient drag and heating reduction devices. However, for some flow conditions and model designs, the flow around spiked bodies can be unstable, which deteriorates their effectiveness. In the present study, a numerical investigation was conducted on a hemispherical body equipped with a spike of variable length and a hemispherical aerodisk of variable size in laminar hypersonic freestream conditions. A mechanism is proposed to explain the drag reduction and the cause of flow instability based on the shape of an effective body. In addition, the dependence of drag reduction on the spike's detailed design was investigated. For the models investigated in this work, an optimum aerodisk size produced the minimum drag and this optimum size was found to be inversely proportional to the spike length.

Nomenclature

b	=	arc length of half a semicircle, m
C_D	=	drag coefficient
D	=	main body diameter, m
d	=	aerodisk diameter, m
L	=	spike length, m
M	=	Mach number
P	=	pressure, Pa
q	=	dynamic pressure, Pa
Re	=	Reynolds number
S	=	surface area, m^2
s	=	distance along the surface, m
T	=	temperature, K
V	=	flow velocity, m/s
β	=	inclination of separation shock wave
γ	=	specific heat ratio
η	=	efficiency of compression
θ	=	inclination of the dividing streamline
μ	=	dynamic viscosity, $kg/m \cdot s$
ρ	=	density, kg/m^3

Subscripts

d	=	value inside the recirculation zone
inf, ∞	=	freestream value
o	=	total, stagnation value
p	=	peak value
r	=	reattachment value
ref, π	=	reference value

I. Introduction

CONCEPTUALLY, when a high-speed flow moves past a blunt body, it experiences a sudden deceleration through a bow shock wave created in front of the body. Downstream of the shock wave, the flow loses most of its kinetic energy and attains large increases of local pressure and temperature, yielding a high drag and heat transfer on the body. Accordingly, there has been an increasing effort to reduce the high drag and heating levels through altering the flowfield pattern in the vicinity ahead of the blunt nose. Among a variety of techniques, attaching a spike at the tip of the hypersonic vehicle proved to be an efficient and simple way to accomplish a significant reduction in both drag and aerodynamic heating [1]. The main features of flowfield around a spiked blunt body are illustrated in Fig. 1. The fundamental idea of introducing the aerospikes is to replace the strong detached bow shock created ahead of the blunt body, shown in Fig. 1a, with a much weaker oblique shock wave attached at the spike tip, shown in Fig. 1b. If a disk of a small size (called the aerodisk) is attached at the spike tip, a much smaller bow shock wave is created detached from the aerodisk, shown in Fig. 1c. It has been proved that a spike with an aerodisk overperformed the plain pointed aerospike in terms of drag and aerodynamic heating reduction [1–4].

In addition to replacing the strong shock wave with a weaker oblique shock, the aerospike works as a "flow separator." Under the influence of an adverse pressure gradient ahead of the body and friction on spike surface, the boundary layer adjacent to the spike surface detaches at a distance from the body nose. Consequently, a large recirculation zone with low pressure and temperature levels "screens" a considerable portion of the body surface area and yields drag and heating reduction [5]. The recirculation zone is enveloped by a shear layer extending from the detachment (separation) point to the reattachment zone, where the local pressure and aerodynamic heating attain relatively higher levels. Because of deflection of flow outside the shear layer, a shock wave is created at the separation point. In cases in which separation occurs at the spike tip/aerodisk shoulder, this shock can coincide with the shock ahead of the spike. Moreover, another shock wave, called the reattachment shock, is created at the reattachment zone to turn the flow outside the shear layer in a direction parallel to the body surface. The strength of the reattachment shock depends on the flow turning angle, which is dictated by the location of reattachment zone on the body surface. In fact, the flow conditions at the reattachment zone dictate the overall performance of the aerospike [5]. The oblique shock ahead of the spike/ aerodisk tip was given different terms in the literature, such as conical shock wave [6,7], bow shock [2], and flow separation shock [1]. Nevertheless, this shock can be conical or bowed (depending on the spike tip geometry) and can take place at or upstream of the separation point. Hence, to avoid confusion, the term "foreshock" is introduced here to refer to the shock wave at the spike/aerodisk tip, whereas the term "separation shock" is used to refer to the shock wave created due to shear layer separation.

Received 8 August 2009; revision received 3 November 2009; accepted for publication 10 November 2009.

*Ph.D. Research Student, Department of Mechanical Engineering, Mappin Street.

†Professor of Aerodynamics, Department of Mechanical Engineering, Mappin Street. Associate Fellow AIAA.

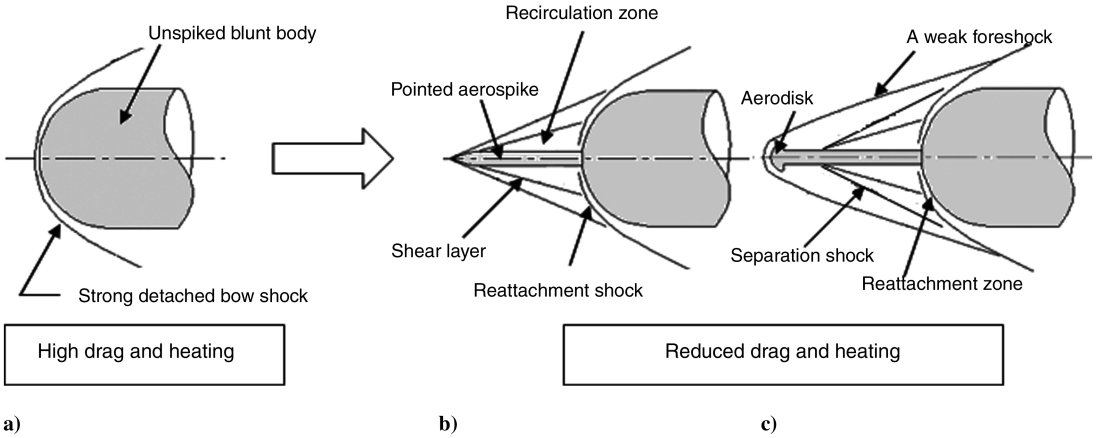

Fig. 1 Features of the flowfield around unspiked and spiked blunt bodies at hypersonic speeds.

If the flowfield maintains a fixed pattern with time, the flow is considered stable. However, for certain geometries of bodies and spikes and under certain flow conditions, there arises a strong possibility of flow instability characterized by a continuously changing flow pattern in a self-exited, self-sustained manner. According to the degree of instability, unstable flow around spiked bodies can be divided into two modes, namely, pulsation and oscillation (the terminology used in Kabelitz [8]). Pulsation mode is characterized by a dramatic change in the shape of the foreshock from conical to hemispherical accompanied by strong variations in the shape of the recirculation zone, high local pressure amplitudes on the body surface, and a high oscillation frequency. On the other hand, the main characteristics of oscillation mode are smaller lateral changes of the shape of the foreshock, along with the shear layer, from concave to convex; lower local pressure amplitudes on the body face; and a lower oscillation frequency. The effectiveness of spike as a drag and heat transfer reduction device and the status of flow stability are governed mainly by the spike design (for the same flow conditions).

Since their introduction to high-speed vehicle design as a drag reduction device in 1940s [9], spikes have been extensively studied over the years. A survey focusing on previous investigations involving hemispherical bodies only is presented here. On the one hand, the impact of spike length on the spike's performance was studied by many researchers. For instance, Mair [10] examined the flowfield around hemisphere cylindrical models equipped with pointed spikes of variable lengths (with a spike length-to-model-diameter ratio, L/D, of up to 6) in laminar supersonic ($M_\infty = 1.96$) flow conditions. In addition, Crawford [11] measured the drag and heat transfer on hemisphere cylindrical models in both laminar and turbulent hypersonic flows ($M_\infty = 6.8$). All models were equipped with pointed spikes with lengths ranging up to $L/D = 4$. The experimental investigation by Crawford was reproduced numerically by a number of researchers, for example, Yamauchi et al. [12], Mehta [13,14], and Asif et al. [15]. Holden [5] measured the heat transfer to spiked hemisphere cylindrical models in turbulent hypersonic ($M_\infty = 10$, 15) flow conditions. All spikes were pointed and their lengths varied up to $L/D = 4.5$. It is noted that all these studies focused on pointed spikes. Nevertheless, hemispherical and flat aerodisks along with pointed spikes in a turbulent hypersonic ($M_\infty =$ 6) flow were recently investigated experimentally by Kalimuthu et al. [3] and reproduced numerically by Mehta [4]. The aerodisks had a fixed size and the L/D varied up to 2.

On the other hand, the role of spike tip and aerodisk design was investigated experimentally and numerically. Heubner et al. [2] conducted experimental investigation of the drag and heat transfer on a hemisphere-capped cylindrical model in a turbulent hypersonic ($M_\infty = 6.06$) flow. The model was equipped with a flat aerodisk fitted to a spike of a fixed length ($L/D = 3$). The effect of the spike's tip shape was investigated experimentally by Milicev and Pavlovic [16]. They focused on measuring the aerodynamic coefficients of a hemisphere cylindrical model equipped with a spike of length $L/D=$ 1 in a turbulent supersonic ($M_\infty = 1.89$) flow. They concluded that a spike with a rounded rather than a pointed tip would produce the maximum drag reduction. Their experiments were reproduced numerically by Asif et al. [15]. Gnemmi et al. [17] investigated three different aerodisk designs, namely, flat, spherical, and biconical disks, used with a spike of a fixed length ($L/D = 1$) and a hemisphere cylindrical model. The investigation involved experimental measurements along with numerical simulations. The flat aerodisk was found to produce the least drag. Kurbatskii and Montanari [18] numerically investigated the same models previously examined in [2,17].

It is noted that all these studies focused on studying the role of aerodisk shape, and the spike length was limited to a fixed value. Only recently, Gauer and Paull [19] conducted a thorough numerical investigation of a spiked blunt conical body in hypersonic speeds. The effect of varying the spike length ($L/D =$ 1:4) and flight speed ($M_\infty = 5$, 7, and 10) were studied. The spikes had pointed and rounded tips, and an aerodisk of two different sizes was examined as well. They concluded that the drag reduction increases monotonically only with longer spikes, whereas it showed nonmonotonic trends with aerodisk size. Nevertheless, the role of aerodisk size and the combined effect of varying both spike length and aerodisk size on the overall performance of the spiked blunt bodies has not been investigated in depth before.

Moreover, flow instability associated with spiked bodies was thoroughly investigated in many studies. However, these studies mainly focused on models in which flow instability is relatively more pronounced, namely, flat cylindrical [20–24] and cone cylindrical models [5,6]. On the other hand, flow instability around spiked hemispherical models gained less attention. Mair [10] and Maull [20] did not record any flow instability associated with such models. However, Crawford [11] indicated signs of foreshock "waviness" in his experiments. Later, in their numerical reproduction of Crawford's experiments, Yamauchi et al. [12] and Mehta [14] reported flow instabilities. Yamauchi et al. [12] recorded a periodic variation of the drag coefficient, which was claimed to be caused by the unsteady vortices inside the recirculation zone. On the other hand, Mehta [14] recorded periodic pressure variation on both spike and body surfaces, which was argued to indicate self-sustained flow oscillations. Nevertheless, no comprehensive investigation on the occurrence of flow instability around hemisphere cylindrical bodies, its cause, mechanism, and the associated range of model designs has been conducted so far.

The purpose of this work is to contribute to the following aspects. First, to investigate the mechanism of drag reduction associated with hemispherical models equipped with aerodisks. Second, to study the combined effect of varying both the spike length and aerodisk size on the level of drag reduction. In addition, to find the design limits for optimum performance (under certain flow conditions). Finally, to study the criteria of flow stability around the models investigated in the present work. The remainder of this paper is arranged as follows. In the next section, the problem of concern is illustrated. Aspects of the numerical approach and related validation studies are then

discussed. The main results are presented and discussed near the end of the paper, which ends with the main conclusions.

II. Problem Description

A. Models' Design

The models studied in this work represent the forebody of a generic spiked hypersonic vehicle, including a main body, a spike, and an aerodisk. The main body is a hemisphere of a unit diameter $D = 1$, the spike is a thin cylindrical rod of variable length and a fixed diameter of $0.05D$, and the aerodisk is a hemisphere of a variable diameter d. To ensure the same penetration of the freestream ahead of the main body regardless of the aerodisk size, the overall length of the spike and the aerodisk is L; see Fig. 2.

A total of 45 designs were investigated in this work. The models have L/D ratios of 0.5, 1.0, 1.5, 2.0, and 2.5 with aerodisk diameter ratios, d/D, varying from 0.0 to 0.4 with a step of 0.05. A value of $d/D = 0.0$ corresponds to a spike (alone) with a sharp conical tip of a 10 deg semi-apex angle. In addition, $d/D = 0.05$ corresponds to a spike (alone) with a rounded tip.

B. Freestream Conditions

Freestream conditions are taken corresponding to a flight speed of $M_\infty = 6$ of zero incidence at an altitude of 60 km above sea level in a standard atmosphere [25]. The freestream values of temperature, pressure, density, and dynamic viscosity are $T_\infty = 247.021$ K, $P_\infty = 21.95$ Pa, $\rho_\infty = 3.0968 \times 10^{-4}$ kg/m^3, and $\mu_\infty = 1.5844 \times 10^{-5}$ kg/m $\cdot$ s, respectively. Accordingly, the freestream velocity is $V_\infty = 1890.3$ m/s. Based on the main body diameter and freestream conditions, the Reynolds number value is $Re_{D\infty} = 3.69 \times 10^4$; the flow is assumed to be laminar.

III. Aspects of the Numerical Investigation

A. Computational Domain

Because of symmetry, an axisymmetric flowfield is studied. Preliminary investigations showed that imposing the undisturbed far field at 1/3 and 1 diameter in the upstream and lateral directions, respectively, is sufficient to capture all foreshocks. Because only the forebody of the hypersonic vehicle is considered, the flowfield is bounded downstream by the nose shoulder, where a pressure outlet boundary is imposed. No-slip conditions are imposed at the solid walls, whereas symmetry conditions with zero normal gradients are assigned at the axis. The flowfield is discretized using a structured grid in four blocks; see Fig. 2.

B. Flow Solver

The numerical investigation is performed using the FLUENT flow solver. This code solves Navier–Stokes equations using the cell-centered finite volume approach. In the present work, a double-precision laminar axisymmetric density-based solver is used. Initially, all 45 cases are solved using the steady time-independent solver. The Courant–Friedrichs–Lewy number and underrelaxation factors are tuned to obtain solution convergence to steady state. Both the numerical residuals and the total drag coefficient are used to monitor the convergence. In cases in which the steady state shows flow instabilities (in terms of varying drag coefficient), the solution so obtained is switched to the unsteady time-dependent solver. The physical time step is set to 1×10^{-3} s, and 20 iterations per time step are performed.

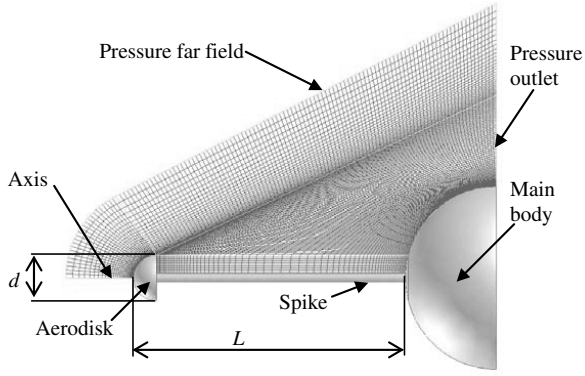

Fig. 2 Model geometry and the computational domain details.

Table 1 Variation of pressure drag coefficient with mesh resolution

Source	Coarse	Medium	Fine	Very fine	[11]
Pressure drag coefficient	0.323	0.291	0.219	0.211	0.21

To validate the numerical solver, one case from the experimental investigations by Crawford [11] is selected. The model is a hemisphere cylinder of $L/D = 2$, and the freestream Mach and Reynolds numbers are $M_\infty = 6.8$ and $Re_{\infty D} = 0.13 \times 10^6$, respectively. Crawford integrated the absolute pressure along the model to calculate the pressure drag coefficient. To test the grid sensitivity, four grids with different resolutions were examined. The coarse, medium, fine, and very-fine grids contained approximately 45,000, 80,000, 250,000, and 350,000 cells, respectively. The pressure drag coefficients calculated using these grids are listed in Table 1 along with the experimental values.

In addition, the pressure variation along the hemispherical part of the model as calculated based on the four grids is plotted in Fig. 3a. The fine and the very-fine grids yielded almost the same pressure distribution. However, the very-fine grid produces a better accuracy compared with the measured pressure distribution [11]. In addition, density gradient contours as predicted by the flow solver based on the very-fine grid are compared with the schlieren photograph of the experiment in Fig. 3b. Features of flow around the model, including

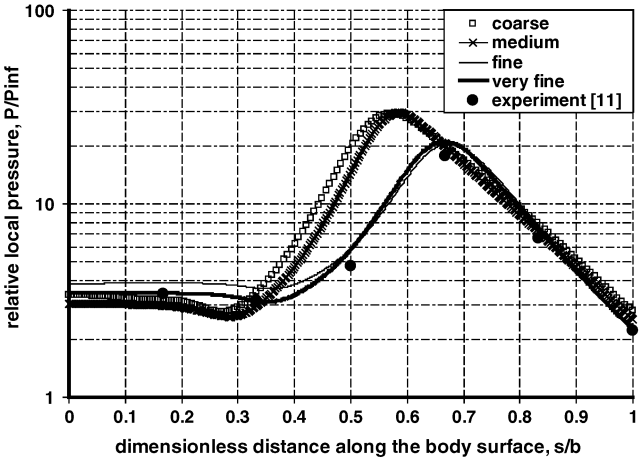

a)

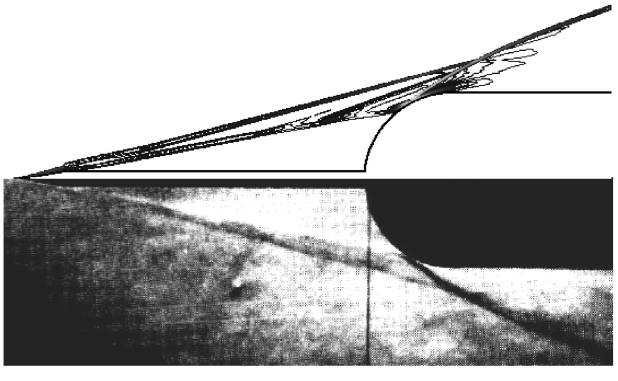

b)

Fig. 3 Results of grid sensitivity and validation tests.

the foreshock, reattachment shock, and shear layer, are accurately predicted.

IV. Results and Discussion

A. Features of the Flowfield

The features of the flowfield around a model with $L/D = 1.5$ and $d/D = 0.15$ are illustrated in Fig. 4.

In this case, the boundary layer detaches at the aerodisk shoulder and the separation shock coincides with the foreshock. The streamline that emanates at the separation point and propagates downstream until it stagnates on the main body surface at the reattachment point (in steady flow conditions) is called the dividing streamline [6] (the term was first introduced by Chapman et al. [26]). The streamlines above the dividing streamline pass downstream, whereas the streamlines below it are trapped inside the recirculation zone. Details of the separation zone are illustrated in the close-up view in Fig. 4a. In addition, the flow pressure maintains a near-constant value in the entire recirculation zone. Nevertheless, as the shear layer approaches the main body surface, the flow decelerates through a compression wave, causing the pressure to increase in the vicinity of the reattachment point. Details of the reattachment zone are shown in the close-up view in Fig. 4b. Immediately behind the reattachment shock, the pressure attains a maximum value, P_p, which is slightly higher than that at the reattachment point, P_r [26]. The curved surface of the hemispherical body causes the flow to expand downstream of the reattachment point through an expansion wave. Hence, the surface pressure decreases toward the main body shoulder. Both the main body and the reattachment shock wave are totally enveloped by the aerodisk shock wave.

The flowfield around models with pointed spikes has almost the same features. Figure 5 illustrates the flow pressure contours (upper half) and velocity contours (lower half) around a model with pointed spike of the same length, $L/D = 1.5$, along with a close-up at the spike's tip. Unlike the aerodisk case, separation takes place downstream of the spike tip shoulder and the separation shock merges with the strong foreshock emanating at the spike tip, forming one shock with a conical shape (rather than the bowed shape of the aerodisk model). The pressure contours at the reattachment point clearly indicate the relatively stronger reattachment shock compared with that of the aerodisk case.

The presence of the main body creates an adverse pressure gradient along the spike that encourages the boundary-layer separation and the creation of the shear layer [20]. Hence, the location of the separation point depends mainly on the spike length [10,20]. To illustrate this, two models with a longer spike ($L/D = 2.5$) and the

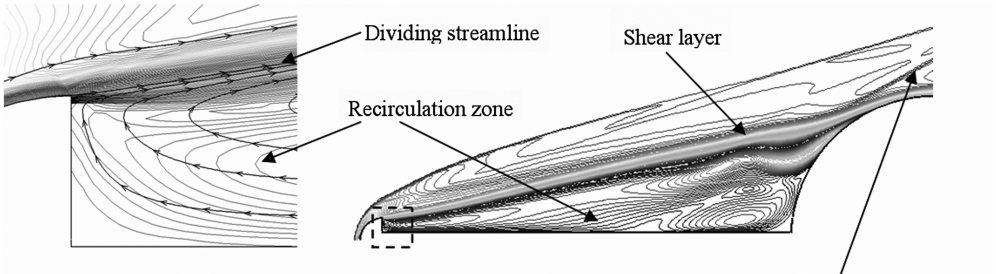

a) Velocity contours

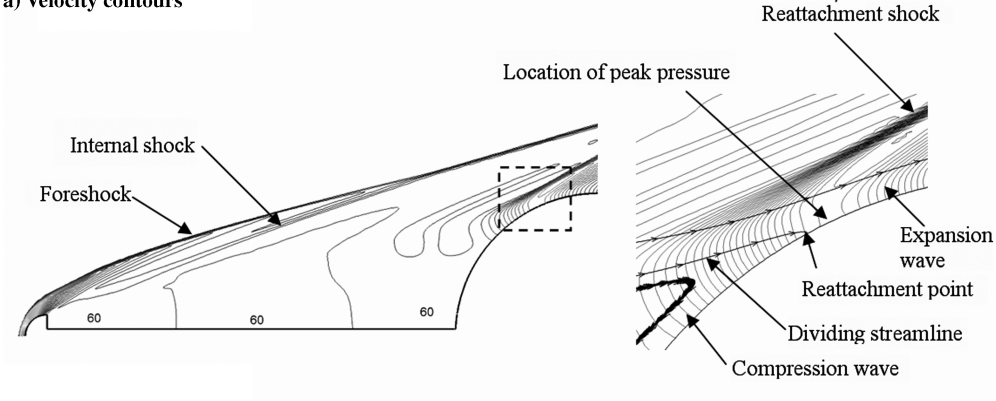

b) Pressure contours

Fig. 4 Features of the flowfield around a model with $L/D = 1.5$ and $d/D = 0.15$.

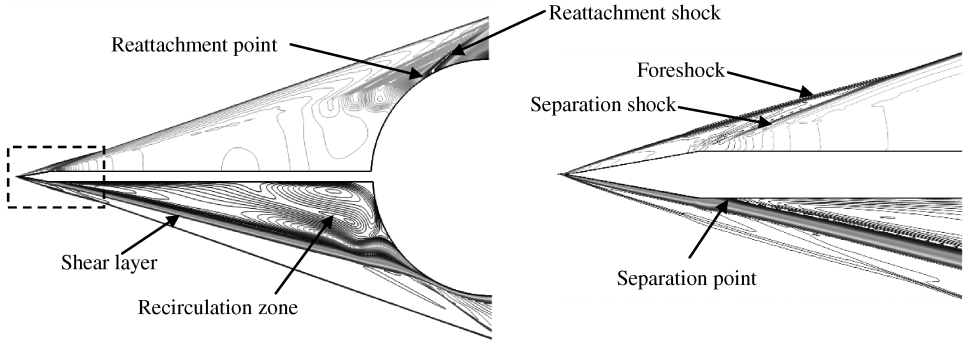

a) The whole flowfield b) A close-up at the spike tip

Fig. 5 Features of the flowfield around a model with pointed spike.

same tip shapes, namely, an aerodisk with $d/D = 0.15$ and a pointed tip, are examined in Figs. 6a and 6b, respectively. The upper half of Fig. 6 illustrates the velocity contours, whereas the lower half illustrates the pressure contours of the flowfield around these models. A close-up at the spike tip in both cases is illustrated in Figs. 6c and 6d, respectively. Closely examining Fig. 6c, the shear layer separates at the aerodisk shoulder and reattaches to the spike immediately downstream of the aerodisk base, whereas in Fig. 6d the boundary layer remains attached to the spike surface. In addition, an expansion wave is created at the tip/aerodisk shoulder to turn the flow outside the shear layer in a direction parallel to it (the size of this expansion fan is larger in the aerodisk case). Then, the shear layer separates from the spike at a distance downstream and the separation shock can be clearly distinguished from the foreshock.

However, by increasing the aerodisk size for the same spike, the shear layer becomes less likely to reattach to the spike after departing from the aerodisk shoulder. For relatively large aerodisks, the shear layer propagates directly toward the main body. Figure 7 illustrates the flowfield around a model with $L/D = 2.5$ and $d/D = 0.4$. The velocity and pressure contours are illustrated in the upper and lower halves, respectively.

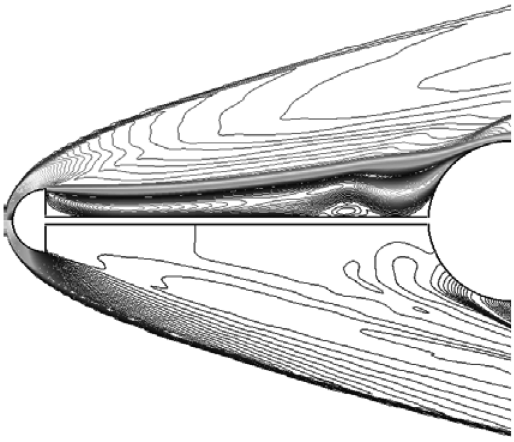

Fig. 7 Flowfield of a model with $L/D = 2.5$ and $d/D = 0.4$.

B. Mechanism of Drag Reduction

1. Models with Sharp Spikes

The drag reduction experienced by spiked blunt bodies was explained by the size of the recirculation zone, which screens a considerable portion of the main body [1,3,12]. Increasing the spike length causes the reattachment point to move further downstream along the main body surface and the recirculation zone to expand, covering a larger area of the main body; consequently, a further drag drop is achieved. As will be shown later, this current hypothesis of drag reduction mechanism fails to fully explain a number of phenomena. Hence, in the present study, an attempt is made to introduce another explanation based on the effective body.

Mair [10] argued that the shape of the recirculation zone was nearly conical; hence, the flow outside the shear layer was very similar to a conical flow. He confirmed this explanation by comparing the inclination angle of separation shock with that ahead of a conical body with the same deflection as the shear layer. These angles were found to be very similar. Crawford [11] confirmed the same explanation and stated that "the flow boundary of the hemispherical-cylinder was then effectively transformed to a flow more nearly like that of a cone-cylinder." Hence, the blunt body is replaced by an effective conical body drawn by the shear layer. Yamauchi et al. [12] explicitly used the "effective body" term to refer to the shape of the shear layer.

However, defining the effective body by the shear layer may not be precise. This is because the thickness of the shear layer increases significantly with distance from the separation point. Chapman et al. [26] estimated the rate of a laminar shear layer thickness growth by about three times that of the attached boundary layer. The growth rate would increase in the event of transition to a turbulent shear layer. In addition, at reattachment, part of the streamlines constituting the shear layer continued moving past the reattachment zone and merged

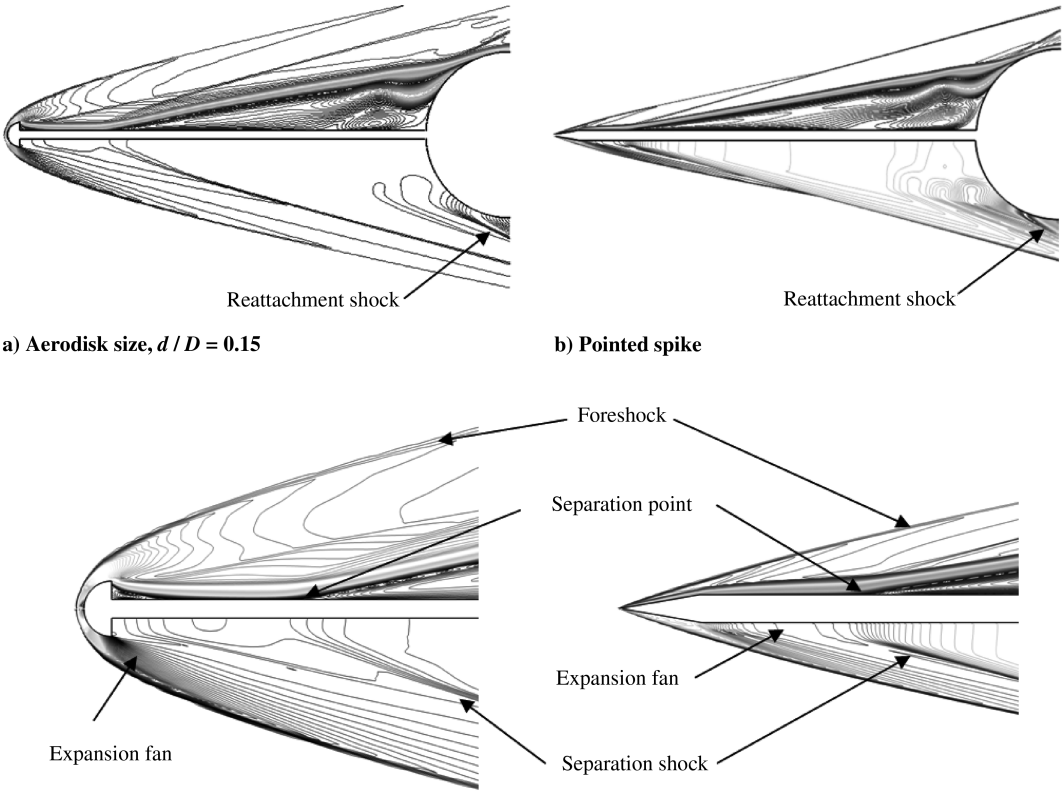

a) Aerodisk size, $d / D = 0.15$ **b) Pointed spike**

c) A close-up at the aerodisk **d) A close-up at the pointed tip**

Fig. 6 Features of the flowfield around two models with long spikes, $L/D = 2.5$.

with the flow downstream of the reattachment shock, whereas the other part was reversed into the recirculation zone. Wood [6] emphasized that, at equilibrium, the dividing streamline links the separation and reattachment stagnation points. In addition, as shown in Fig. 4, the location of peak pressure on the main body surface is associated with the location of the dividing streamline reattachment point. Moreover, it was shown [22,24] that the stability of this streamline dictates the overall stability of the flowfield. Figure 8 illustrates more details about the dividing streamline of a typical model with a pointed spike ($L/D = 2$).

The pressure contours in Fig. 8a also show that the locations of both the separation and reattachment shocks are associated with both ends of the dividing streamline. In addition, the straightness of the latter for most of its length indicates that the flow pressure experiences very small gradients along and across the shear layer. However, as the dividing streamline approaches the main body surface, it slightly deflects under the influence of the reattachment shock. This yields the creation of an internal expansion fan ahead of the reattachment zone. The velocity contours in Fig. 8b show the details of boundary-layer evolution at the spike's sharp tip. As argued by Wood [6], the dividing streamline starts from stagnation at the shear layer separation point and restagnates at the reattachment point on the main body surface at equilibrium. Figure 8c also shows that, although the streamlines are very close to each other, they either escape downstream or reverse into the recirculation zone. Only the dividing streamline completely stagnates at the body surface. Hence, we find it more accurate to use the dividing streamline rather than the shear layer to define the outer profile of the effective body.

To validate this hypothesis, the dividing streamlines for three models with pointed spikes, namely, $L/D = 1.5$, 2.0, and 2.5, are investigated. As will be shown shortly, models with $L/D = 0.5$ and 1.0 experience unstable flow. Thus, they are not studied here. The inclination angles of the dividing streamline and separation shock are compared with the theoretical analysis of supersonic flow around conical bodies [27] in Fig. 9. The comparison shows good agreement of the hypothesis with the theoretical relations.

Figure 9 also suggests that increasing the spike length yields a more slender effective body (smaller θ). The resulting weaker foreshock yields a lower downstream pressure field. Figures 10a and 10b illustrate the pressure variation for the three models along the spike surface and main body surface, respectively. The horizontal axis in Fig. 10a represents the distance measured from the conical tip shoulder, whereas in Fig. 10b it represents the normalized distance along the main body surface measured from spike root. P_{ref} is used in Fig. 10b (and in the remainder of this paper) to refer to the pressure value at the stagnation point of the reference (unspiked) model under the same freestream conditions.

In Fig. 10a, the initial pressure drop is caused by the expansion fan immediately after the spike's tip shoulder, whereas the abrupt subsequent pressure rise is caused by the separation shock. Clearly, at equilibrium, the distance to separation increases and the required

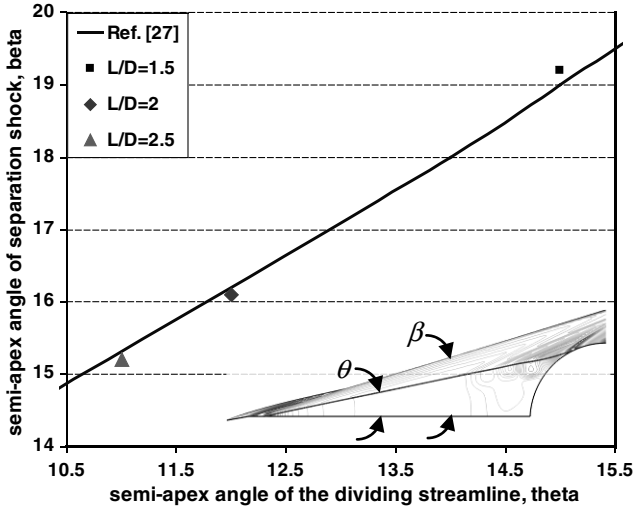

Fig. 9 Inclination of the dividing streamlines and separation shocks in models with pointed spikes.

pressure for separation decreases by increasing the spike length, which is consistent with the previous analysis [20]. Nevertheless, the distance from separation to the main body increases by increasing the spike length. Increasing the spike length also pushes the reattachment point of the dividing streamline slightly toward the main body shoulder; see Fig. 10b. Overall, the inclination angle of the effective body, θ, decreases. Moreover, the required flow deflection, the strength of the reattachment shock, and, consequently, the peak pressure, P_p decrease by increasing the spike length. In Fig. 10b, the pressure rise and the subsequent drop are caused by the compression and expansion waves created in the reattachment zone; see Fig. 4b. Figure 10b also declares that, regardless of the spike length, the peak pressure on the main body surface is significantly less (at least 72.5% lower) than the stagnation pressure on the same body under the same freestream conditions without using the spike (reference pressure).

2. *Models with Aerodisks*

The mechanism of drag reduction using aerodisks is not clear from previous investigations so far. Moreover, the relative potential superiority of aerodisks in drag reduction compared with pointed spikes was not explained either. In fact, because the aerodisk generates a bowed foreshock, this superiority may seem unexpected. Guenther and Reding [28] suggested that the small region of circulating flow (created at the wake of the aerodisk) merges with the main recirculation zone ahead of the blunt body and forms a larger zone of separated flow that results in a larger drag reduction compared with that produced by a plain spike alone. However, it will be shown that the drag is reduced regardless of this merge. Here, an attempt is made

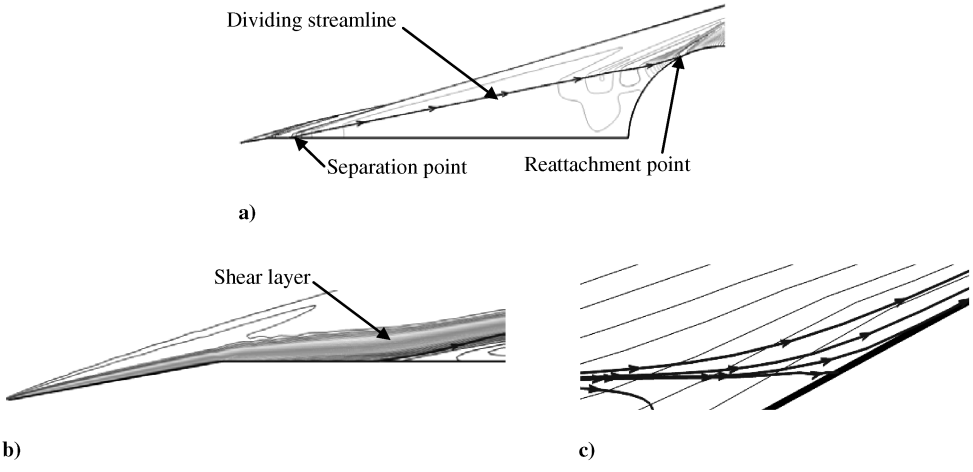

Fig. 8 Details of the dividing streamline.

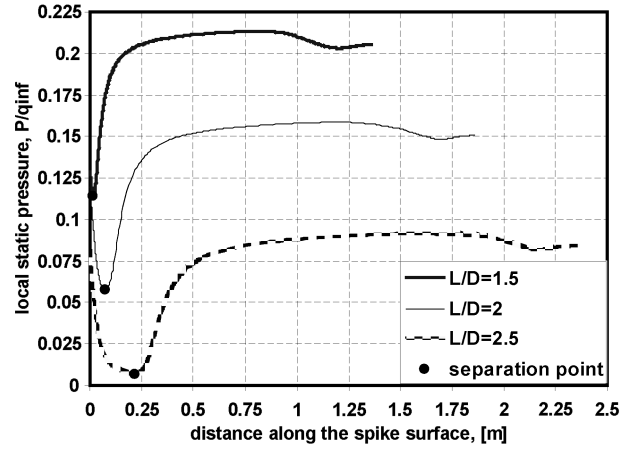

a) Along the spike surface

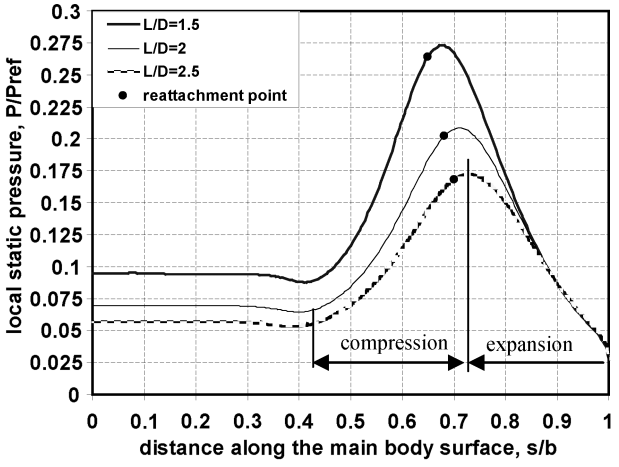

b) Along the main body surface

Fig. 10 Surface pressure variation for three different models with pointed spikes.

to explain the mechanism and superiority of aerodisks in reducing drag. Our hypothesis of the effective body based on the dividing streamline is employed for the explanation of the drag reduction mechanism in models with aerodisks.

Figure 11a illustrates the variation of local pressure along the main body of four models with a spike length of $L/D = 1.5$ and different aerodisk sizes. For comparison, the corresponding pressure distribution for a model with a pointed spike of the same length is also plotted. Figures 11b–11e show the shape of the effective body as outlined by the dividing streamline. It can be shown that increasing the aerodisk size pushes the separation point (which is located at the aerodisk shoulder) further away from the body axis. Nevertheless, the reattachment point is shifted further toward the main body shoulder. However, the overall effect of increasing the aerodisk size is that the inclination of the dividing streamline is reduced and (with a fixed spike length) the effective body becomes more slender. It can be argued that the effect of the strong bowed foreshock is local and limited to the smaller aerodisk surface and that the expansion fan at the aerodisk shoulder acts to reduce the downstream pressure field. Consequently, the main body is not affected by the strength of the foreshock. Moreover, it can be deduced that the size of the expansion fan (and, hence, the pressure drop across it) increases with the aerodisk size because the dividing streamline inclination decreases at the separation point.

By closely examining Fig. 11, three more remarks can be made. First, in the model with $d/D = 0.4$, the reattachment point is shifted slightly upstream. This may be explained assuming that, at equilibrium, the local pressure field at the reattachment zone imposes the reattachment location that ensures the stability of the dividing streamline. Nonetheless, the peak pressure is further reduced. This is mainly caused as a consequence of a low pressure field downstream of the relatively larger expansion fan created at the aerodisk shoulder. Second, in the models that have spikes with rounded tips, $d/D = 0.05$, the dividing streamline emanates from the separation point that is located on the spike at a distance downstream of the rounded tip. In contrast, in models with larger aerodisks, $d/D >$ 0.05, separation takes place at the aerodisk shoulder. Boundary-layer separation in this case is enhanced by the combined role of the expansion fan (lower pressure of the dividing streamline) and the vicinity of the main body (higher adverse pressure gradient). However, as will be shown later, there exist some cases in which the boundary-layer separation takes place on the aerodisk tip surface. Finally, a spike with a rounded tip ($d/D = 0.05$) provides a pressure reduction compared with the spike with a pointed tip. Clearly, replacing the pointed spike tip with a rounded one shifts the separation point slightly upstream. Hence, the associated effective body becomes slightly more slender. To illustrate this, a close-up of the separation zone of both models is shown in Fig. 12.

This role of aerodisk size as discussed earlier continues for longer spikes as well. However, for relatively longer spikes, slight differences in the flowfield can be distinguished. Figure 13a illustrates the variation in flow gauge pressure with the distance along the spike's surface for three models with the same spike length, $L/D = 2.5$, and different aerodisk sizes along with the pointed spike. In all models, the distance is measured along the cylindrical part of the spike and, for better illustration, only the front half of the spike is considered. Generally, the flow pressure decreases monotonically with an increase in the aerodisk size. However, a slightly different trend is witnessed in the vicinity of the aerodisk–spike junction.

Gauge pressure variation along the spike surface of a model with an aerodisk size $d/D = 0.1$ in the vicinity of the aerodisk is separately plotted in Fig. 13b, whereas the gauge pressure contours in the same zone are illustrated in Fig. 13c. The dividing streamline that outlines the effective body is shown in a thick dashed line. Initially, the flow pressure at the aerodisk base area significantly decreases below the freestream value (a negative gauge pressure). This is caused by the large expansion fan at the aerodisk shoulder imposed by the shape of the effective body. This large expansion fan manages to reduce the high pressure levels caused by the foreshock. However, the dividing streamline inclination decreases gradually as it approaches the spike surface. This creates a shock wave that is responsible for the subsequent pressure increase until it reaches a local peak value (at nearly $0.05L$ from the aerodisk base). The dividing streamline moves parallel to the spike surface. In this phase, the shear layer reattaches on the spike surface and the flow pressure slowly decreases. Finally, as the shear layer detaches again from the spike surface, the separation shock is created, and the flow pressure increases again.

The influence of the large expansion fan is still evident for larger aerodisks ($d/D = 0.25$). However, the length of shear layer attachment on the spike surface is significantly reduced. Figure 14a shows the gauge pressure contours and the dividing streamline for this model. Clearly, the shape of the effective body implies a continuous pressure rise downstream of the expansion fan at the aerodisk shoulder.

A further increase in aerodisk size ($d/D \geq 0.3$) further reduces the tendency of the dividing streamline to be directed toward the spike surface. Hence, the size of the expansion fan decreases such that the flow pressure drop across it is reduced. Figure 14b illustrates the gauge pressure contours and the effective body outline for this model. It is important to note here that the gauge pressure at the aerodisk base attains a positive value, which indicates that the local absolute pressure is higher than the freestream pressure. It can be assumed that the small expansion fan is incapable of restoring the pressure levels after the strong foreshock.

3. Factors Governing the Effective Body Shape

According to the hypothesis presented in this work, the effective body is outlined by the dividing streamline. In models that have spikes with pointed ($d/D = 0.0$) or rounded ($d/D = 0.05$) tips, the

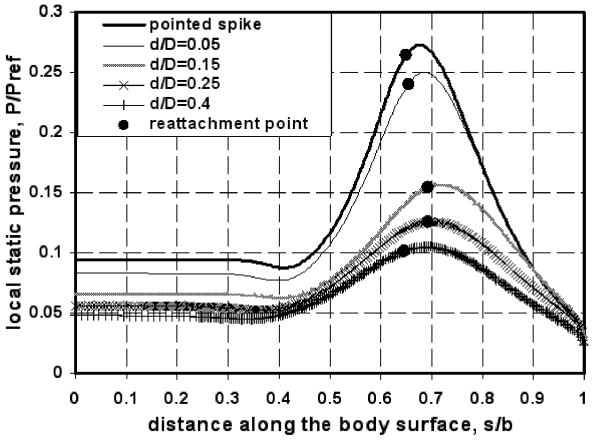

a)

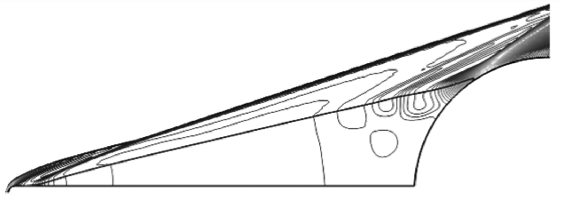

b) $d / D = 0.05$

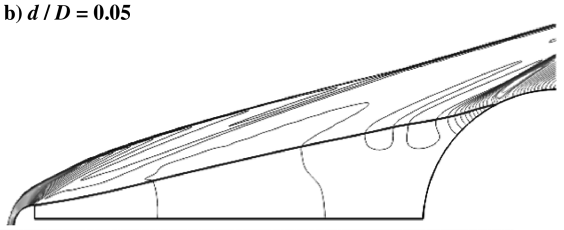

c) $d / D = 0.15$

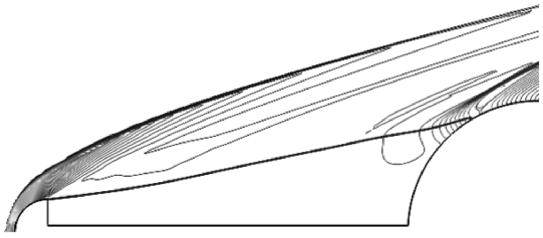

d) $d / D = 0.25$

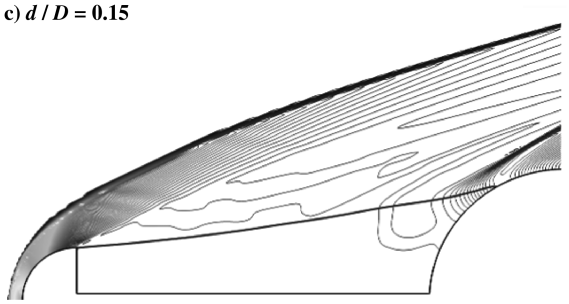

e) $d / D = 0.4$

Fig. 11 Impact of aerodisk size on the shape of the effective body.

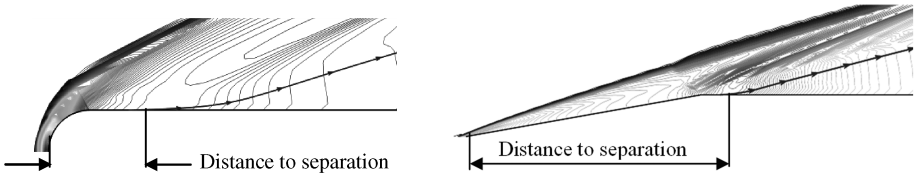

a) rounded spike **b) pointed spike**

Fig. 12 Close-up at the separation zone of two models with the same spike tip size.

dividing streamline is almost a straight line. Consequently, the effective body associated with these models has a conical shape; see Figs. 15a and 15b. The shear layer created on the spike surface remains attached to it until it separates under the influence of the adverse pressure gradient as the shear layer approaches the main body.

In contrast, in the models equipped with aerodisks ($d/D > 0.05$), the shear layer separates at the aerodisk shoulder. According to the spike length and aerodisk diameter, the shear layer may propagate directly toward the main body or have a more curved profile. Hence, the shape of the effective body as determined by the dividing streamline varies from one model to the other; see Figs. 15c and 15d. In this section, the factors dictating the geometry of the effective body are discussed.

Chapman et al. [26] suggested that the parameter that dictates the flow pressure inside the recirculation zone and, hence, its size is the total pressure along the dividing streamline in the vicinity of reattachment zone. He argued that, for a stable flow, the total pressure of the dividing streamline is equal to the peak static pressure at reattachment. Thus, at equilibrium, the pressure of a stable flow inside the recirculation zone, P_d, is related to the reattachment pressure, P_r:

$$P_d = \frac{P_r}{\eta(1 + \frac{\gamma-1}{2}M^2)^{\gamma/(\gamma-1)}} \tag{1}$$

where M is the value of the Mach number along the dividing streamline and the compression efficiency factor, and

$$\eta = P_r/P_o \tag{2}$$

represents the effects of viscosity on the compression of the dividing streamline. P_o is the total pressure of the dividing streamline as it approaches the reattachment zone. This stability criterion was implemented by Kenworthy [21] as the cause of the oscillation mode around spiked flat cylindrical models. His approach was confirmed numerically by Feszty et al. [23].

Here, an attempt is made to extend these hypotheses. The assumption is that, at equilibrium, the shape of the effective body is dictated by the energy level of the dividing streamline immediately downstream of the separation point. More precisely, dividing streamlines that possess high energy levels (mainly pressure) immediately downstream of the separation point manage to proceed directly to the reattachment point on the main body surface. On the other hand, dividing streamlines that have low pressures (and, consequently, low energy) get closer to the spike and reattach to it. Hence, depending on the spike length and aerodisk size, local values of Mach number and pressure attain certain values and their combination (in terms of total pressure value) determines the energy level in the dividing streamline and eventually dictates the outlines of the effective body. To validate this assumption, the dividing streamline of the models with the same spike length ($L/D = 2.5$) are investigated. Figure 16 illustrates

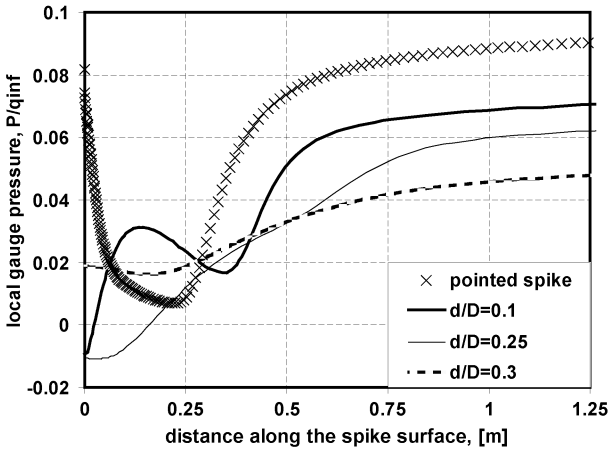

a)

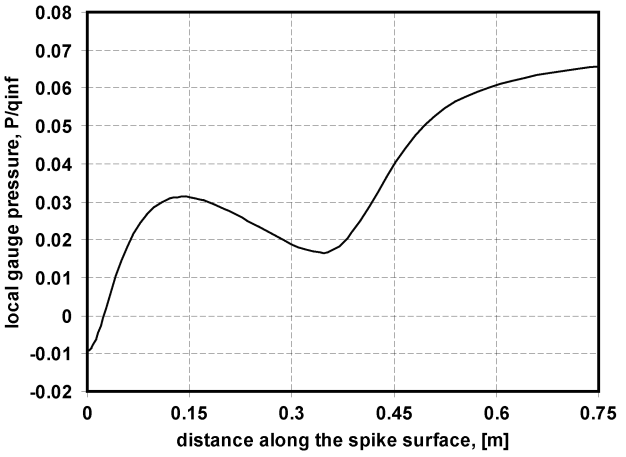

b)

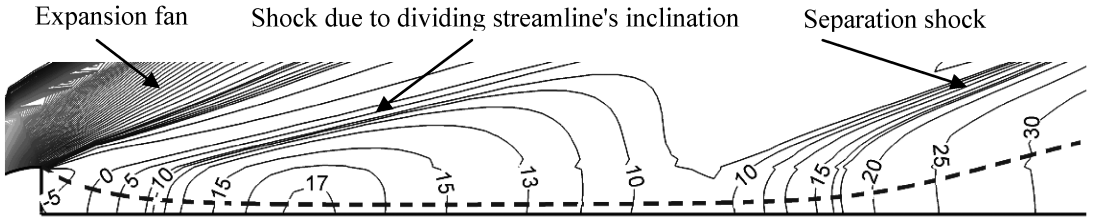

c)

Fig. 13 Variation of flow gauge pressure for a model with $L/D = 2.5$ and $d/D = 0.1$.

the evolution of the shape and total pressure along the dividing streamline immediately after separation from the aerodisk shoulder.

At equilibrium, the inclination of the dividing streamline dictates the size of the expansion fan at the aerodisk shoulder and, hence, the local values of pressure at the aerodisk base. Hence, models with large aerodisks yield dividing streamlines that are less inclined with relatively higher energy levels. Thus, they separate at the aerodisk shoulder and do not reattach on the spike's surface. In contrast, the dividing streamlines associated with small aerodisks start with low energy levels and they reattach on the spike's surface immediately after separation from the aerodisk shoulder. Nevertheless, in the latter case, as the dividing streamline approaches the main body, it experiences a pressure rise and eventually manages to separate from the spike and propagate toward the main body. In both cases, the total pressure of the dividing streamline continues, increasing as it passes through the compression wave at the reattachment zone. According to Chapman et al. [26], if the total pressure of the dividing streamline equals the peak pressure downstream of the reattachment shock, the dividing streamline stagnates on the main body and a stable shear layer is attained.

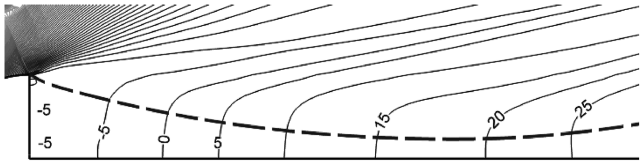

a) $d / D = 0.25$

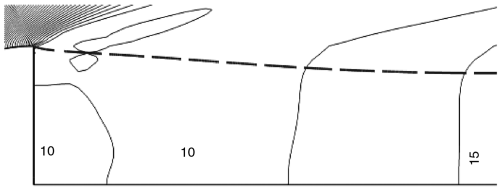

b) $d / D = 0.3$

Fig. 14 Gauge pressure contours downstream of the aerodisk for two models with $L/D = 2.5$.

C. Modes of Flow Around the Spiked Body

The majority of the models investigated in this work showed stable flow features. However, for some models the flow was unstable. The characteristics of the flow modes are discussed in this section.

1. Characteristics of the Stable Mode

A stable flow is characterized by a numerical solution that has fast convergence to the steady state at which the calculated aerodynamic forces no longer change with iterations. The drag convergence history of a typical model with a stable flow mode is shown in Fig. 17.

In addition, the flowfield of a stable flow mode maintains a fixed pattern that does not change with iterations. As suggested by Chapman et al. [26], the fundamental criterion of a stable flow is that the dividing streamline emanating at the separation point is the same dividing streamline stagnating at the reattachment point; see Fig. 18. This only occurs if the energy level of the dividing streamline (in terms of its total pressure) at the reattachment point is sufficiently very close to peak pressure generated by the reattachment shock wave. This pressure balance on both sides of the dividing streamline at reattachment imposes a mass balance. Hence, the dividing streamline keeps a fixed position, and the shape of the effective body (Fig. 18b) remains unchanged. Eventually, the flowfield features as well as the associated drag remain unchanged.

2. Characteristics of the Unstable Mode

On the other hand, the numerical solution of some designs shows significant fluctuations in the aerodynamic forces at steady state. The solution is then switched to the unsteady time-dependent solver with which this unstable performance is more accurately captured.

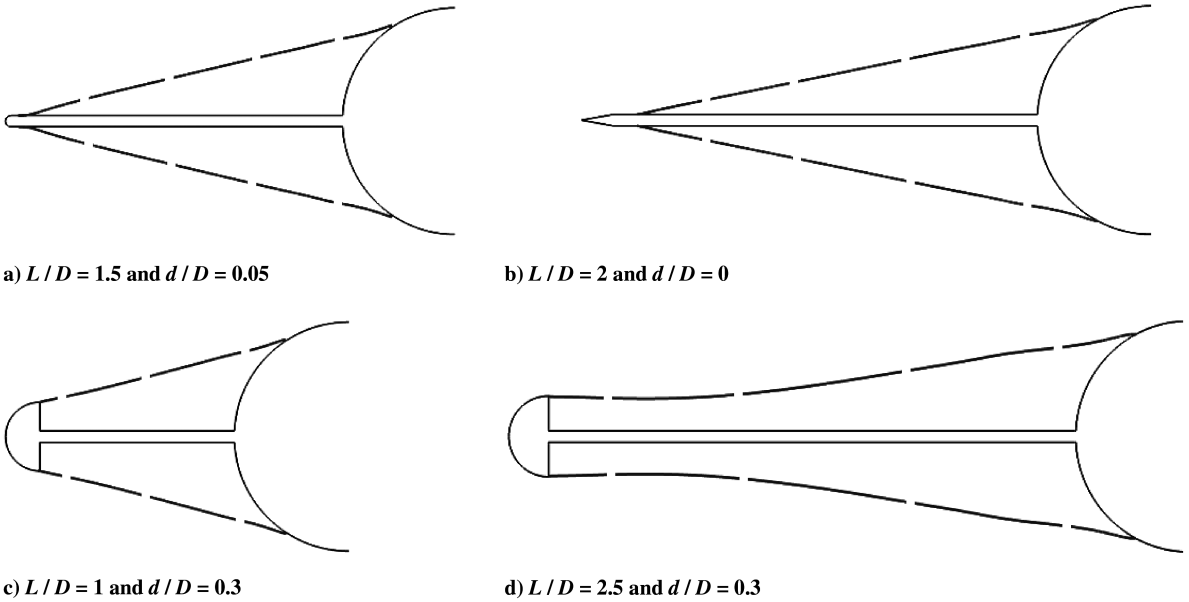

a) $L/D = 1.5$ and $d/D = 0.05$ b) $L/D = 2$ and $d/D = 0$

c) $L/D = 1$ and $d/D = 0.3$ d) $L/D = 2.5$ and $d/D = 0.3$

Fig. 15 Geometry of the effective body outlined by the dividing streamline for four different models.

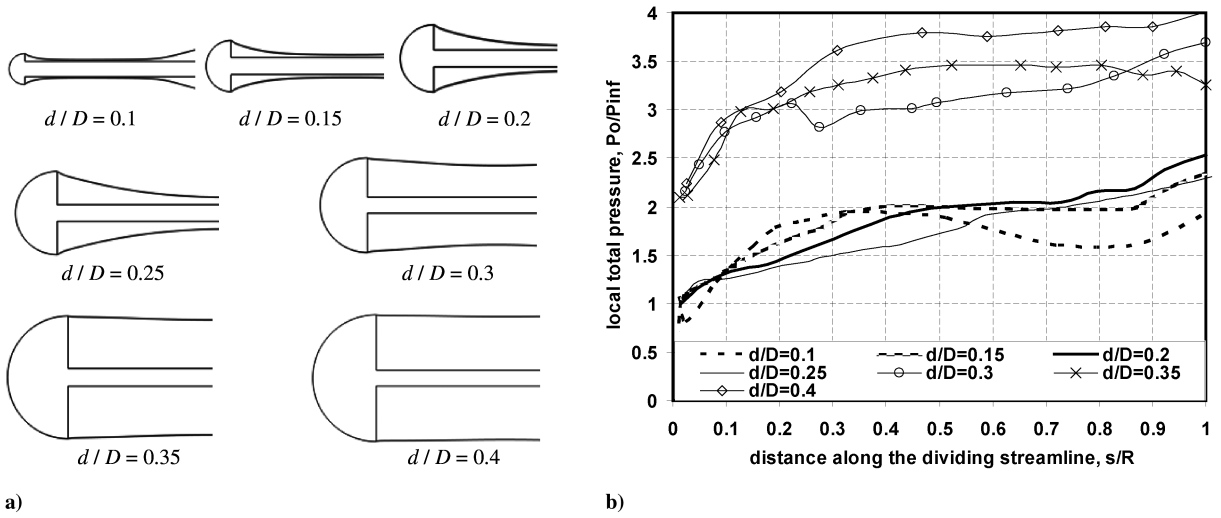

a) b)

Fig. 16 Features of the dividing streamline for models with $L/D = 2.5$: a) shape, and b) total pressure.

Figure 19 illustrates the features of the numerical solution associated with a typical unsteady flow mode as predicted by the unsteady solver.

A typical model with an unsteady flow mode is studied here. It has the spike length of $L/D = 1$ and the aerodisk diameter of $d/D = 0.1$. The flowfield associated with this model continuously changes its pattern with time. Static pressure contours of the unstable flow mode at different instances are shown in Figs. 20a–20i, while their corresponding drag values are plotted in Fig. 20j.

A close examination of Figs. 20a–20i shows that the streamline emanating at the aerodisk shoulder either reverses into the recirculation zone (Figs. 20a–20c) or escapes downstream of the reattachment zone (Figs. 20d–20h) and another streamline reattaches on the main body surface. Because no single streamline links the separation and reattachment points, the term "dividing streamline" is no longer accurate. Feszty et al. [23] introduced the terms "bounding" and "escape" to refer to the streamline emanating from the aerodisk shoulder and the one reattaching on the main body surface, respectively. However, we find it more meaningful to introduce two new terms, namely, "separating" and "reattaching," respectively. Depending on the mutual position of the separating and reattaching streamlines, two different situations can be distinguished.

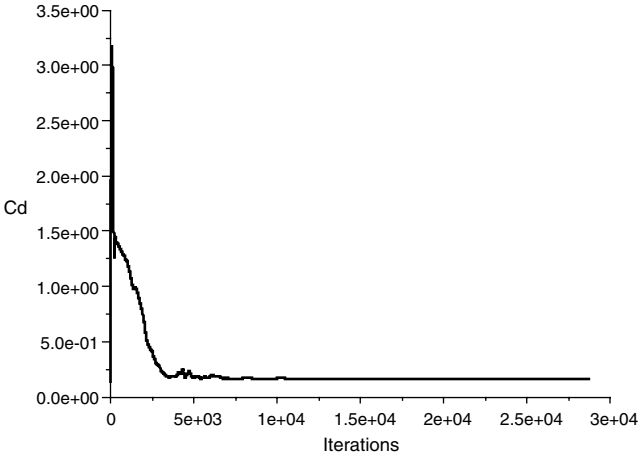

Fig. 17 Features of the numerical solution of the stable flow mode.

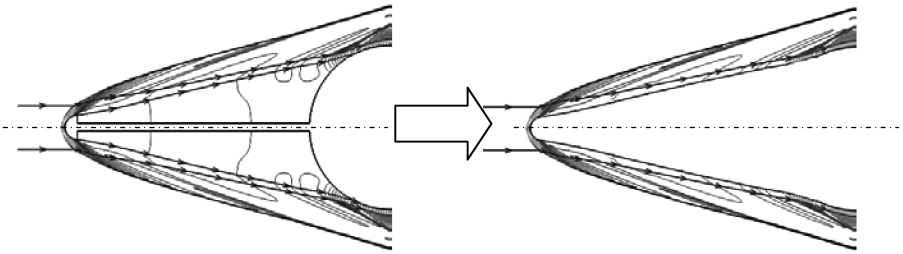

Fig. 18 Criteria of the stable flow mode.

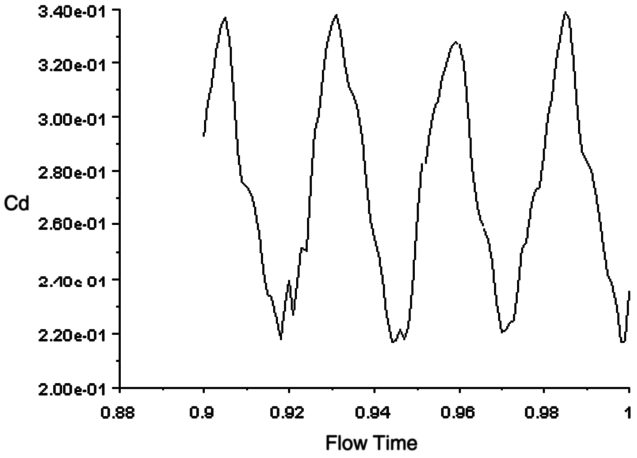

Fig. 19 Features of the numerical solution of the unstable flow mode.

In Figs. 20a–20c, the reattaching streamline originates from the far field and engulfs the separating streamline. The latter then reverses into the recirculation zone. In contrast, in Figs. 20d–20h, the reattaching streamline originates from within the recirculation zone and is engulfed by the separating streamline. The latter manages to escape downstream along the reattachment zone. In either situation, the location and, hence, the strength of the reattachment shock wave are dictated by the stagnation location of the reattaching streamline (reattachment point).

3. Mechanism of Flow Instability

The flow instability can be explained as follows. At a certain instance, the inclination of the dividing streamline (immediately downstream of the separation point) dictates its pressure and, hence, its total pressure. However, as it propagates downstream, its velocity and, hence, its total pressure increase. According to Chapman et al. [26], if the total pressure of the dividing streamline is less than the peak pressure at the reattachment zone, it cannot proceed toward the stagnation point; rather, it reverses into the recirculation zone forming a separating streamline. Another streamline with higher total pressure (coming from the freestream with higher velocity) manages to stagnate at the reattachment point on the main body, forming a reattaching streamline (Fig. 20a). This pattern of the streamlines corresponds to a net mass inflow to the recirculation zone [26]. As mass flows into the recirculation zone, the separating streamline is pushed outward and the recirculation zone slightly inflates starting from right (compare Figs. 20a and 20b). This mass inflow also yields a pressure rise in the flow ahead of the body. The inflation and pressure rise have the effect of adding more energy (total pressure) to both the separating and reattaching streamlines as they approach the reattachment zone. As a consequence of this energy increase, the separating streamline manages to proceed further into the reattachment zone (Fig. 20c). On the other hand, equilibrium implies that the reattaching streamline (with higher energy) stagnates at a point closer to the spike root, yielding a stronger reattachment shock, a higher peak pressure, and, consequently, a higher drag. As a consequence, the foreshock moves further toward the spike. Eventually, the separating and reattaching streamlines come closer to each other and the amount of mass inflow diminishes and is finally cut off. The evolution of the flowfield pattern in this phase (Figs. 20a–20c) is summarized in the schematic in Fig. 21.

Drag continues increasing until it attains a maximum value and the foreshock becomes closest to the body in Fig. 20d. In spite of mass inflow cut off, the previously injected airstream continues moving inside the recirculation zone in the upstream direction (note the pressure contours' gradient in Figs. 20b and 20c). The injected airstream causes the inflation of the recirculation zone to move further upstream; consequently, the foreshock starts to move away from the body (starting from Fig. 20e). This airstream also increases the flow pressure immediately downstream of the aerodisk and the separating streamline gains more energy (total pressure). If the total pressure possessed by the separating streamline exceeds the peak reattachment pressure, it manages to escape past the reattachment zone [26]. Another streamline with lower energy (originating from the recirculation zone with lower velocity) stagnates at the reattachment point and forms the reattaching streamline.

This arrangement of streamlines corresponds to a net mass outflow of the recirculation zone [26]. On the other hand, the separating streamline continues moving further away from the spike and gaining more energy. Eventually, the gap between the separating and reattaching streamlines increases; consequently, the net mass outflow increases (Figs. 20d–20f), causing a reduction of flow pressure inside the recirculation zone. Hence, the energy level of the separating and reattaching streamlines decrease. Whereas the former comes closer to the body, the latter is pushed away from the body to ensure a more appropriate (lower) stagnation pressure (Figs. 20f–20h). Consequently, the reattachment shock becomes weaker, drag decreases, the two streamlines come closer to each other, and the air outflow diminishes and, eventually, is cut off (Fig. 20h). As the separating streamline loses energy, it no longer becomes capable of reaching the reattachment point and is reversed again into the recirculation zone (Fig. 20i), where the drag attains a minimum value and the foreshock is farthest from the body. The cycle then continues from Fig. 20i to Fig. 20a, in which the amount of mass inflow increases and decreases after starting from Fig. 20a. The schematic in Fig. 22 illustrates the evolution of the flowfield features from Figs. 20d–20h.

It can be assumed that the transition of the separating streamline from Fig. 20c to Fig. 20d and from Fig. 20h to Fig. 20i occurs almost instantaneously and the separating streamline never reattaches on the main body (the interim time is 2 and 1 ms, respectively). An overview of a complete cycle of oscillation shows that both the shear layer and the foreshock perform a lateral flappinglike motion with small amplitude and low frequency. Kenworthy [21] recorded and explained the same characteristics of oscillation flow mode. However, his investigation focused on flat cylindrical bodies. Here, flow instability of the oscillation mode is extended to hemispherical models, which were not investigated in previous studies.

The mechanism of flow instability as explained here is based upon the status of the energy level (in terms of total pressure) of the dividing streamline. To confirm this assumption, the evolution of total pressure along the separating streamline (S, dashed lines) and the reattaching streamline (R, solid lines) in both Fig. 20d (with no markers) and Fig. 20i (with x markers) are illustrated in Fig. 23. The solid markers indicate the value of peak pressure (P) at the reattachment zone. Clearly, in both situations, the terminal energy level of the reattaching streamline is very close to the peak pressure value. The total pressure of the separating streamline in Fig. 20d is

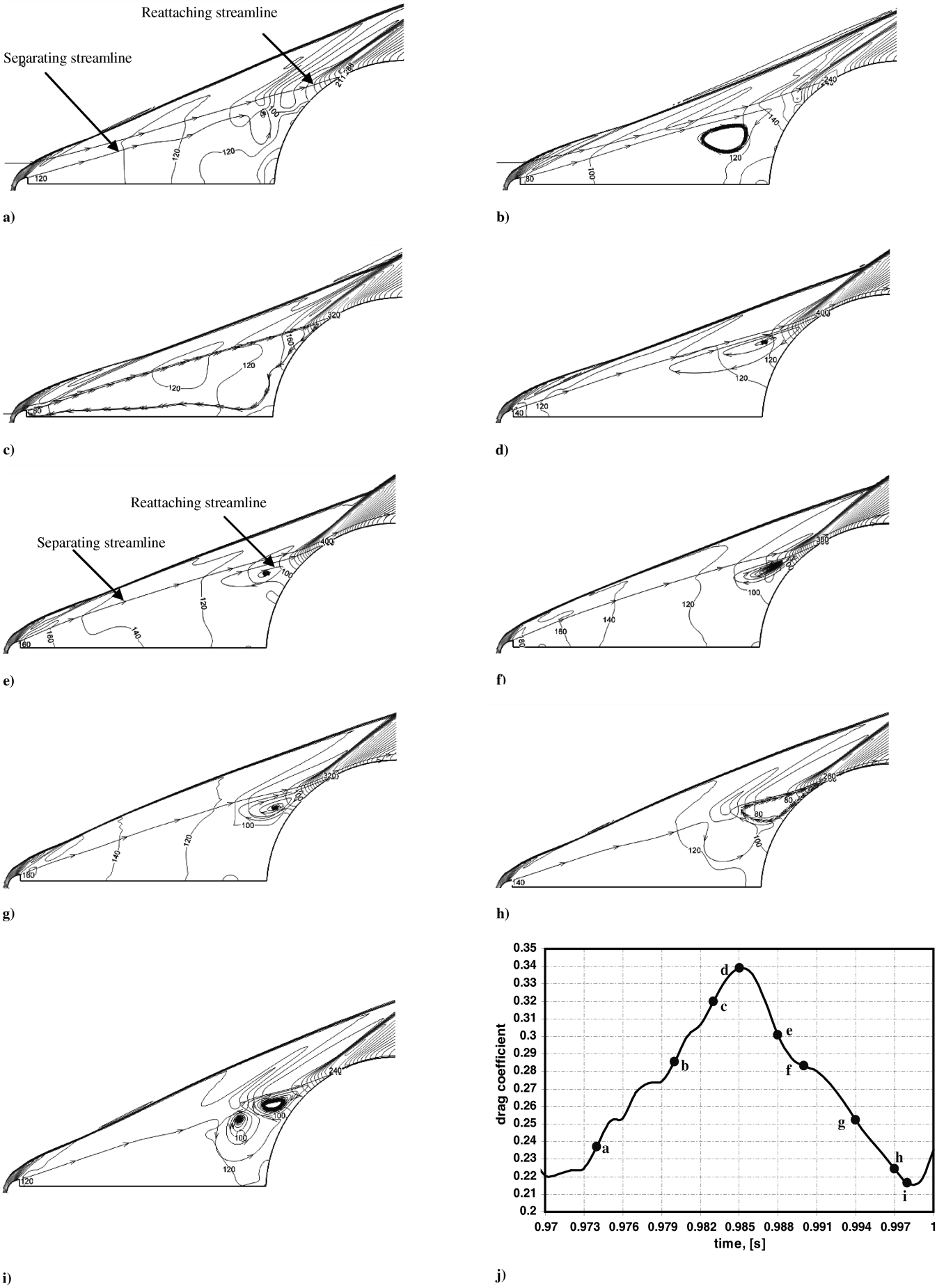

Fig. 20 Variation of flowfield pattern and the corresponding drag in the unsteady flow mode.

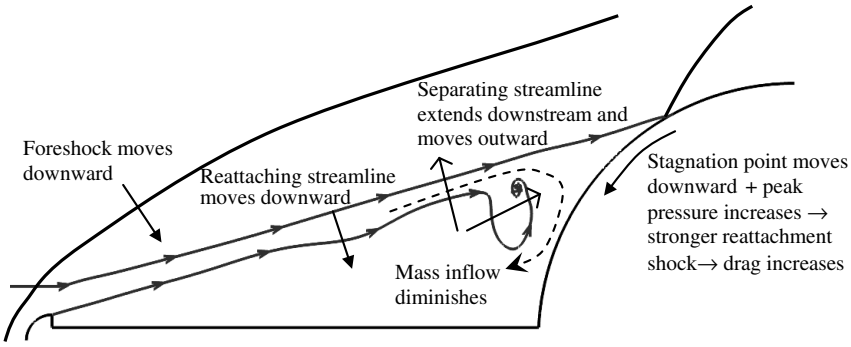

Fig. 21 Evolution of the flowfield from Fig. 20a to Fig. 20c.

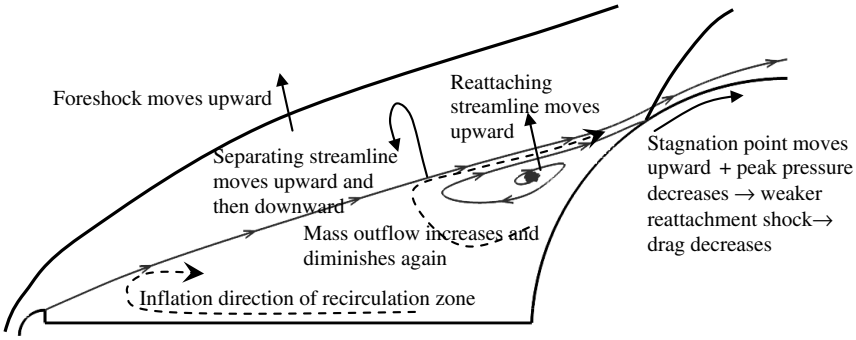

Fig. 22 Evolution of the flowfield from Fig. 20d to Fig. 20h.

higher than the peak pressure at stagnation. In contrast, the separating streamline in Fig. 20i possesses a total pressure that is always below the peak pressure value.

The flow around spiked bodies can be stable or unstable depending on their design. For the models investigated in this work, both spike length and aerodisk diameter dictate the flow mode. Figure 24 illustrates this dependence on the whole design space. Generally, for the specific freestream conditions investigated here, the flow around the spiked model can be stable if the spike length exceeds the main body diameter. More interesting, increasing the aerodisk size can stabilize the flow. Models with $L = D$ experience a stable flow if the aerodisk diameter exceeds 25% of the main body diameter.

D. Variation of Reattachment Pressure with Spike Design

Figure 25 illustrates the values of the reattachment pressure and their location on the main body surface for all the models investigated in this work. For the models experiencing flow oscillation, the mean peak pressure value is used.

For all models, the reattachment pressure is less than the stagnation pressure of the unspiked (reference) model, P_{ref}. Moreover, increasing the spike length shifts the location of reattachment further toward the main body shoulder. This corresponds to a larger portion of the main body being screened by the recirculation zone. In addition, the peak pressure decreases monotonically, with both the spike length and aerodisk diameter. However, their role in reducing the reattachment pressure tends to diminish with increasing dimensions. For instance, the peak pressure on a model with $L = D$ and $d = 0.3D$ would be 26.4% lower if its spike was 50% longer and only 39.6% lower if its spike length was doubled. Similarly, a model with $L = 2D$ and $d = 0.3D$ would experience almost the same peak pressure at the same location with a further increase of its aerodisk size.

E. Drag Components

It may be expected from this discussion that the total drag (mainly pressure drag) would be minimum if both the spike length and

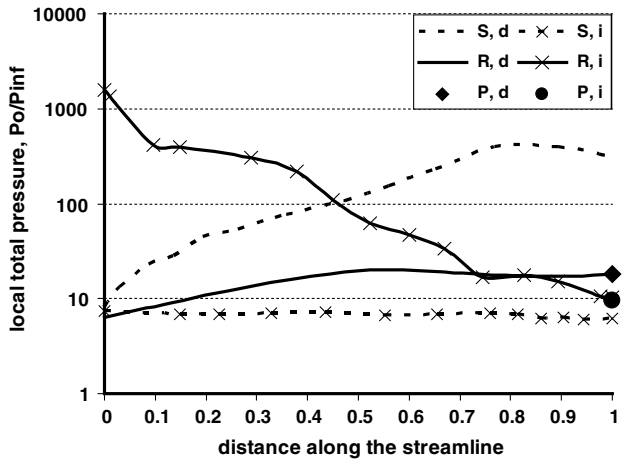

Fig. 23 Evolution of total pressure of the separating and reattaching streamlines in Figs. 20d and 20i.

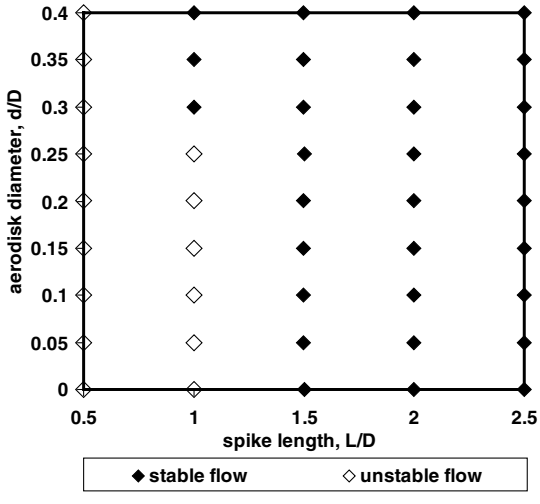

Fig. 24 Dependence of flow stability on spike length and aerodisk size.

aerodisk diameter were maximum. However, considering the complete spiked body geometry, there exist other components of drag, namely, the aerodisk, the spike, and the base of the hemispherical body. Because the models studied here are considered "forebodies" of complete vehicles, the base drag is not evaluated whereas the aerodisk contributes to the drag with two components, namely, its tip and its base; see Fig. 26. In this section, the individual drag components are separately investigated. For models experiencing unsteady flow with varying drag, the average values are used.

1. Main Body

The main body drag follows the expected trend. As the spike and aerodisk dimensions increase, the reattachment point shifts toward the main body shoulder and a larger area of the body surface is screened by the recirculation zone. Overall, the pressure and friction drag on the main body decrease monotonically as both spike length and aerodisk diameter increase; see Fig. 27.

Drag is mainly due to pressure distribution on the main body in all models. The spike length shows a slightly more dominant role in reducing the main body drag. However, this dominance and the overall effectiveness of the spike in reducing the drag diminish for longer spikes and larger aerodisks.

2. Aerodisk Tip

The variation of drag components on the aerodisk tip with spike design is illustrated in Fig. 28.

Similar to the main body, pressure drag is the major drag component on the aerodisk tip. It is independent of spike length (markers referring to models with different spike lengths and the same aerodisk diameter coincide). This can be explained by the fact that the aerodisk maintains a hemispherical shape regardless to its size and is exposed to the freestream regardless of the spike length. Hence, the local static pressure on the tip surface maintains the same distribution. However, as the aerodisk diameter increases, its projected area increases; hence, its pressure drag increases in a parabolic manner; see Fig. 28a. Friction drag follows almost the same trend. However, pointed tips produce slightly higher friction drag compared with rounded tips of the same diameter, $d/D = 0.05$, due to its higher surface area. In addition, models with $L/D = 0.5$ yield a

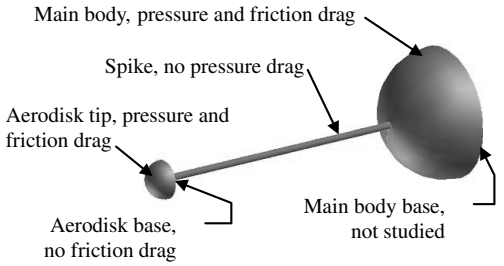

Fig. 26 Elements of drag on the spiked body.

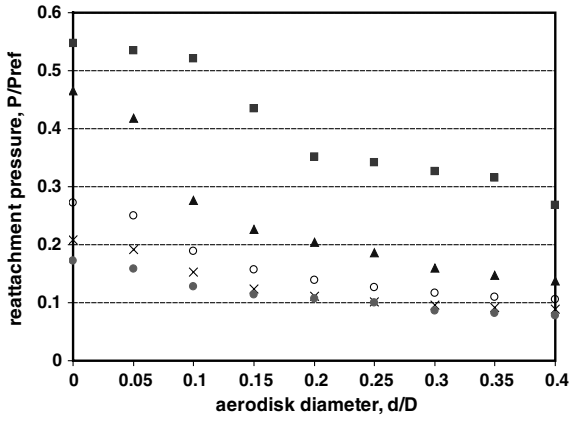

a) Values of reattachment pressure

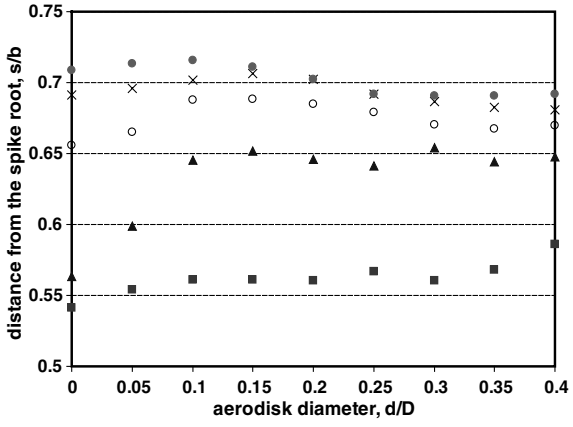

b) Locations of reattachment point

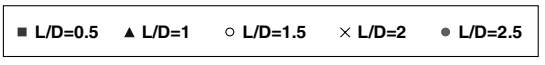

Fig. 25 Variation of reattachment pressure values and locations with models' design.

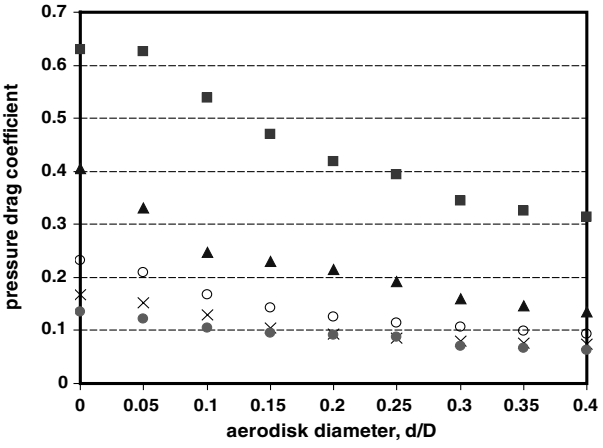

a)

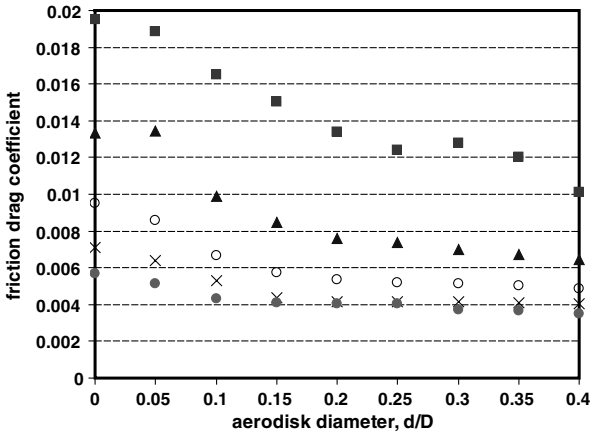

b)

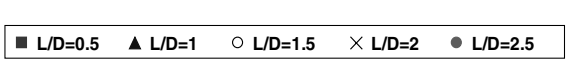

Fig. 27 Variation of drag components on the main body with models' design: a) pressure drag coefficient, and b) friction drag coefficient.

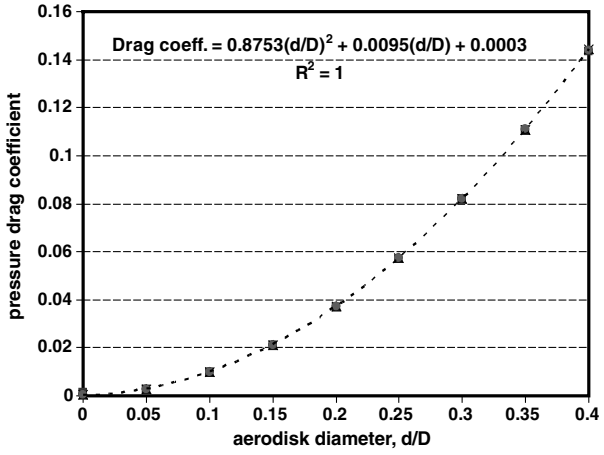

a)

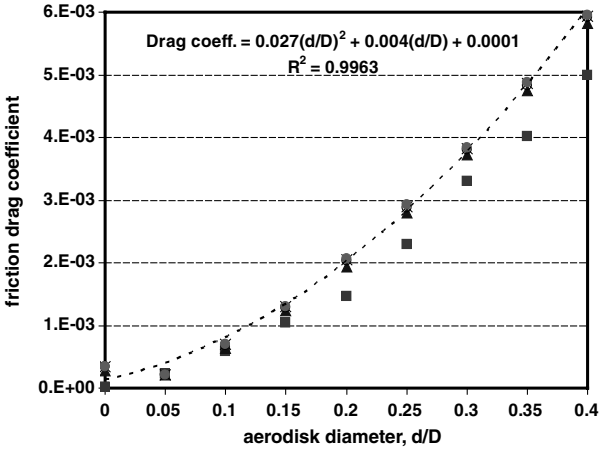

b)

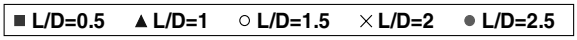

Fig. 28 Variation of drag on the aerodisk tip with models' design: a) pressure, and b) friction.

slightly lower friction drag compared with models with longer spikes, especially with larger aerodisks. This can be explained by the early separation of the boundary layer attached on the aerodisk surface. Hence, a small part of the tip area (downstream of separation) is exposed to negative friction drag. Overall, the total friction drag coefficient is reduced. Figure 29a shows the location of dividing streamline separation on the aerodisk tip surface for two models with the same aerodisk size, whereas Fig. 29b illustrates the variation of wall shear stress along the aerodisk tip surface. The point beyond which the shear stress attains negative values clearly indicates the separation point of the dividing streamline.

3. *Aerodisk Base*

Being normal to the freestream velocity direction, the base of aerodisk has no contribution to friction drag and only pressure drag is generated depending on the local values of gauge pressure at the base. Models with pointed spikes ($d/D = 0$) or rounded spikes ($d/D = 0.05$) have no aerodisk base drag. The variation of aerodisk base pressure drag with the models' design is illustrated in Fig. 30a.

The negative values of aerodisk base drag indicate that its direction is opposite to the freestream velocity, which corresponds to a positive gauge pressure of the flow at the base. Its absolute value, however, increases with the aerodisk size (for the same spike length) due to an increase in the projected area. On the other hand, increasing the spike length (with the same aerodisk diameter) reduces the local gauge pressure at the aerodisk base. Eventually, models with $L/D = 2.5$ and small aerodisk sizes, $d/D < 0.3$, produce positive values of aerodisk base drag. These values (plotted separately in Fig. 30b) indicate that the flow static pressure at the aerodisk base falls below the freestream pressure (negative gauge pressure). However, for larger aerodisks, $d/D \geq 0.3$, the local gauge pressure attains a positive value. This special behavior of aerodisk base drag is mainly due to the shape of the effective body at the aerodisk shoulder. To explain this, Fig. 31 illustrates the gauge pressure contours and the dividing streamline for four different models (Fig. 31d is not to scale).

The inclination of the effective body at the aerodisk shoulder dictates the degree of expansion (pressure drop) of the flow downstream of the foreshock. Thus, models with shorter spikes yield an effective body of a relatively higher inclination, less flow expansion, and, consequently, higher pressure at the aerodisk base; see Fig. 31a. A more slender (less inclined) effective body associated with a longer spike yields further pressure reduction; see Fig. 31b. A further increase in the spike length results in a negative inclination of the effective body, more expansion, and negative gauge pressure at the aerodisk base; see Fig. 31c. However, increasing the aerodisk size in the latter case restores the straightness of the effective body shape, which produces a narrower expansion fan and, eventually, a positive gauge pressure at the aerodisk base; see Fig. 31d.

4. *Spike*

Being parallel to the freestream velocity direction, the spike produces no pressure drag. The variation of the spike's friction drag with the models' design is illustrated in Fig. 32. The behavior of the

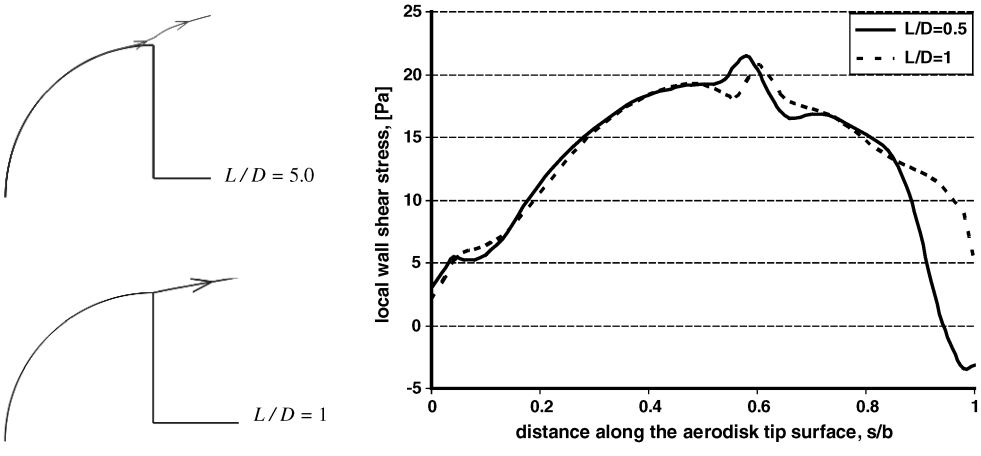

a) b)

Fig. 29 Location of separation point on the aerodisk tip surface for two models with $d/D = 0.4$ and the corresponding wall shear stress.

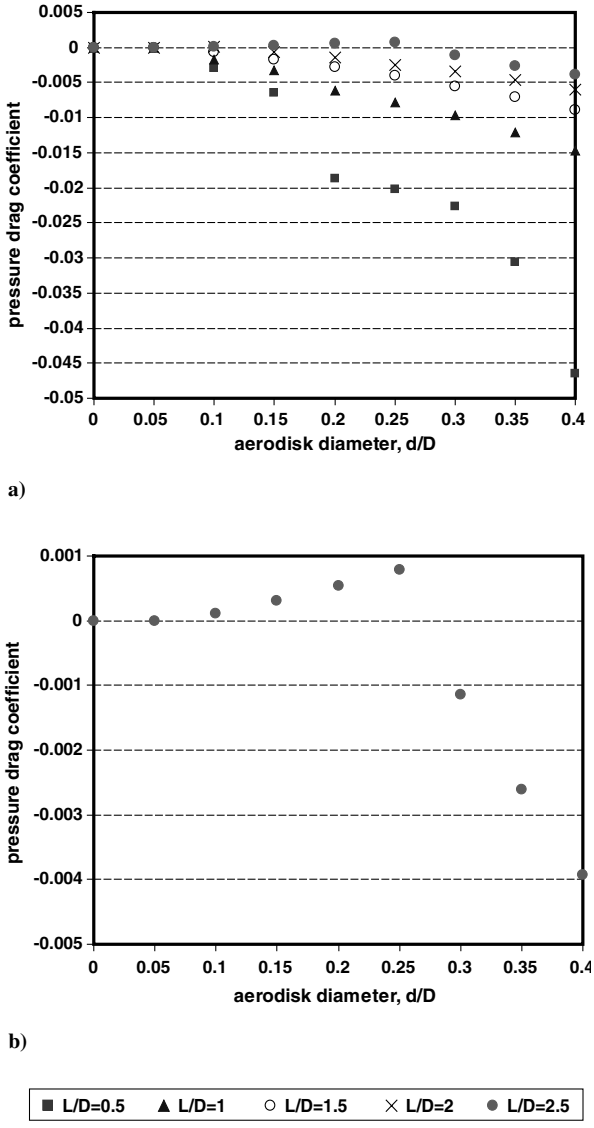

Fig. 30 Variation of aerodisk base pressure drag with models' design.

skin friction drag acting on the spike seems more complicated. It can be positive (which corresponds to a net friction force acting in the direction of freestream velocity) or negative (which corresponds to a net friction force acting opposite to the freestream velocity direction).

However, each curve in Fig. 32 can be divided into three phases, depending on the aerodisk size and regardless of the spike length: an initial rise to a maximum positive value, a subsequent drop to a minimum value (negative in most of the cases), and a final slow rise. Models with $L/D = 0.5$ slightly violate this behavior. This may be explained by the effect of unsteadiness on the flow features inside the recirculation zone.

In the first phase, replacing the pointed tip, $d/D = 0.0$, with a rounded one, $d/D = 0.05$, yields an increase in the friction drag. This can be explained by the shift of the separation point downstream along the spike. Recalling Fig. 12, the distance to separation along the cylindrical spike is larger in Fig. 12a than in Fig. 12b. To illustrate this more clearly, the variation of axial shear stress along the cylindrical spike of length $L/D = 1.5$ with both pointed and rounded tips is plotted in Fig. 33. Indeed, the shear stress is zero exactly at the separation point, positive upstream, and negative downstream. Ahead of the main body, the shear stress becomes positive again.

This can be explained by the flow structure inside the recirculation zone; see Fig. 34. Areas of positive and negative friction drag are marked by plus and minus signs. The slightly larger area associated with rounded spikes also contributes to increasing the skin friction drag coefficient.

The second phase is characterized by a continuous drop in friction drag. It starts with $d/D = 0.05$ and continues for larger aerodisks until a certain size at which the friction drag attains a minimum value. This phase can be better explored by examining the models with $L/D = 2.5$. Figure 35 illustrates the variation of local axial shear stress along the spike with different aerodisk sizes.

As discussed earlier, in models with smaller aerodisks, the shear layer separates on the aerodisk shoulder, reattaches on the spike surface, and separates again from the spike at a distance downstream. A small area of circulating flow is entrapped below the shear layer immediately at the aerodisk base (shown in the insert in Fig. 35a), for which the size increases by increasing the aerodisk diameter (recall Fig. 16). A negative shear stress is generated at this area, which explains the negative values at the beginning of the curves in Fig. 35a. Clearly, the span of this area increases with aerodisk size and the peak shear value is associated with the maximum velocity gradient in the middle of this area. In addition, increasing the aerodisk size shifts the location of both reattachment and separation points on the spike

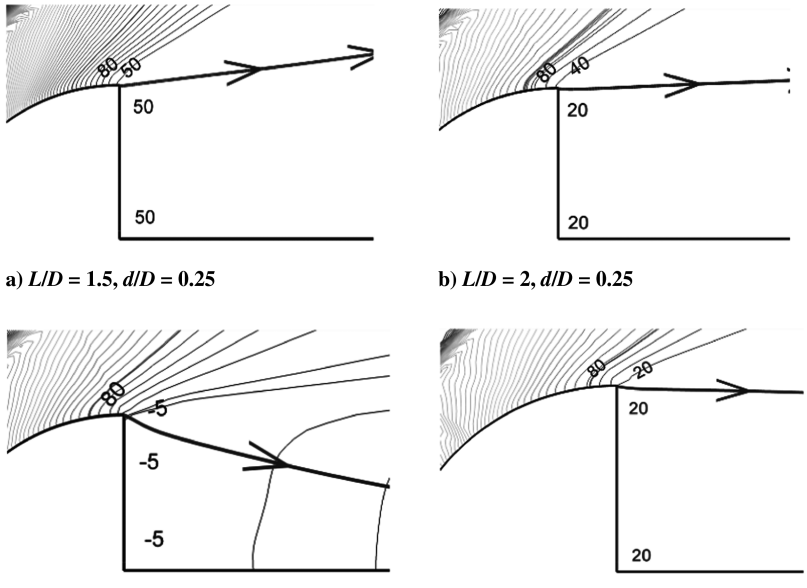

a) *L/D* = 1.5, *d/D* = 0.25 **b) *L/D* = 2, *d/D* = 0.25**

c) *L/D* = 2.5, *d/D* = 0.25 **d) *L/D* = 2.5, *d/D* = 0.35**

Fig. 31 Flow details at the aerodisk base of four different models.

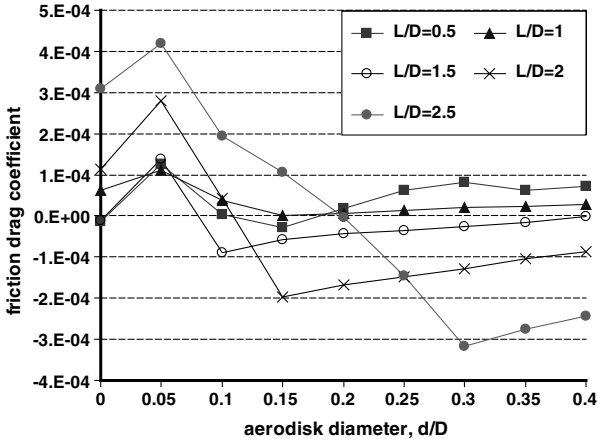

Fig. 32 Variation of friction drag on spikes with models' design.

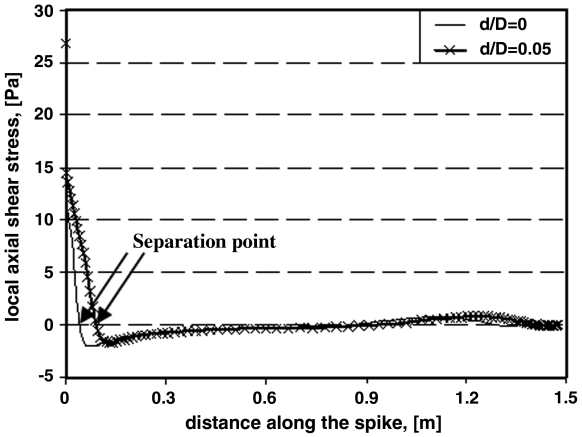

Fig. 33 Variation of axial shear stress along the spike of two models with $L/D = 1.5$.

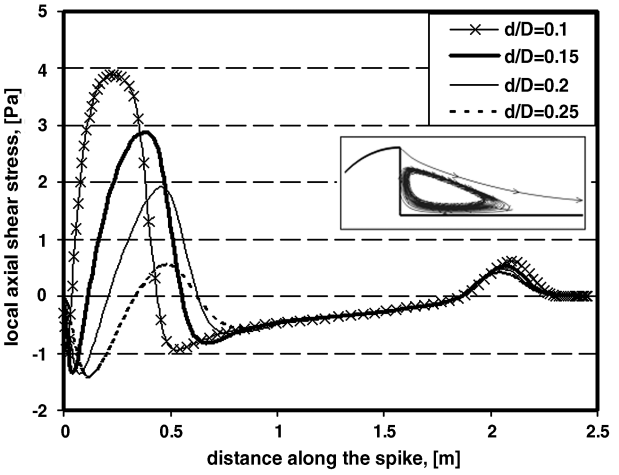

a)

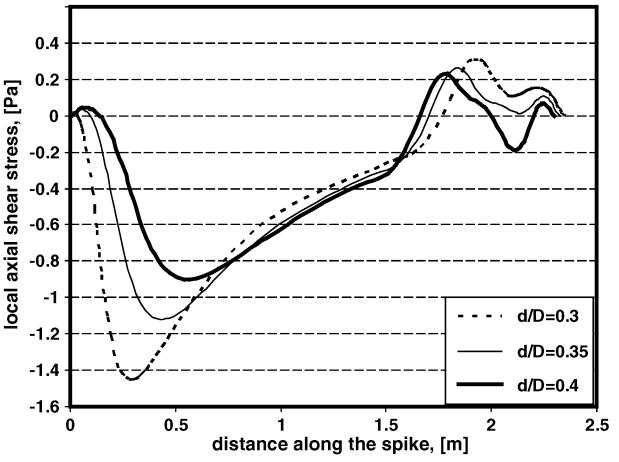

b)

Fig. 35 Variation of local axial shear stress on the spike of models with $L/D = 2.5$.

further downstream and reduces the attachment distance. The span of the subsequent positive shear stress interval is associated with this attachment distance. Moreover, increasing the aerodisk size increases the distance along the shear layer from aerodisk shoulder to reattachment on the spike. Indeed, the velocity gradient across the shear layer decreases with the distance along it. This explains the reduction in peak shear stress in the second phase. Indeed, this reduces the velocity gradients. A negative shear is generated downstream of the separation and, due to the structure of the recirculation zone, a zone of positive shear is created ahead of the main body. Overall, the net effect of positive and negative shear stress (the area under the curves in Fig. 35a) yields a continuous drop of the friction drag by increasing the aerodisk size; eventually, a minimum value is reached at a certain aerodisk size depending on the spike length. This minimum can be positive depending on the sign of shear stress integration. More interestingly, the second phase of a monotonic drop in friction drag is bounded by the aerodisk size at which the shear layer propagates directly toward the main body and does not reattach on the spike.

The third phase is characterized by a slight increase in the friction drag beyond its minimum. Models in this phase have aerodisks large enough for the shear layer to propagate directly to the main body without reattaching on the spike surface. Figure 35b illustrates typical models for $L/D = 2.5$.

It can be assumed that the rise in friction drag value in this phase is caused by the decrease in negative peak shear stress. This may be explained assuming that, as the aerodisk size increases for models in this phase, the volume of the recirculation zone increases and the vortices inside it expand in size. Hence, the velocity gradients decrease; consequently, the peak of shear stress is reduced. The overall effect is a reduction of the negative part of the shear stress and a net increase in the friction drag coefficient.

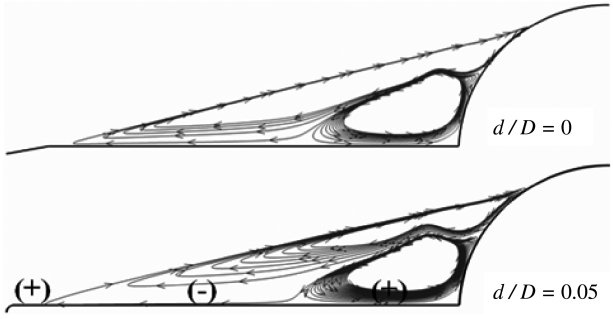

Fig. 34 Flow streamlines inside the recirculation zone of the two models in Fig. 33.

5. *Total Drag Coefficient*

The variation of the net pressure, friction, and total drag coefficients with the models' design is illustrated in Figs. 36a–36c, respectively. The corresponding values associated with the reference (unspiked) body at the same freestream conditions as evaluated by the flow solver are 0.863, 0.024, and 0.887, respectively.

Comparing the individual drag components described earlier, it is clear that drag on the spiked models is mainly due to pressure distribution on both the aerodisk and the main body. Other pressure and friction drag components play minor roles. In all spiked models, a drag reduction is achieved compared with the unspiked model. However, the maximum drag reduction is not associated with the longest spike or the largest aerodisk. Nevertheless, for the same aerodisk size, the longer the spike the less the drag. The dominant role of spike length is still witnessed. A more interesting phenomenon can be addressed from Fig. 37, in which the focus is only on models experiencing a stable flow mode (models with $L/D > 1$). Clearly, for

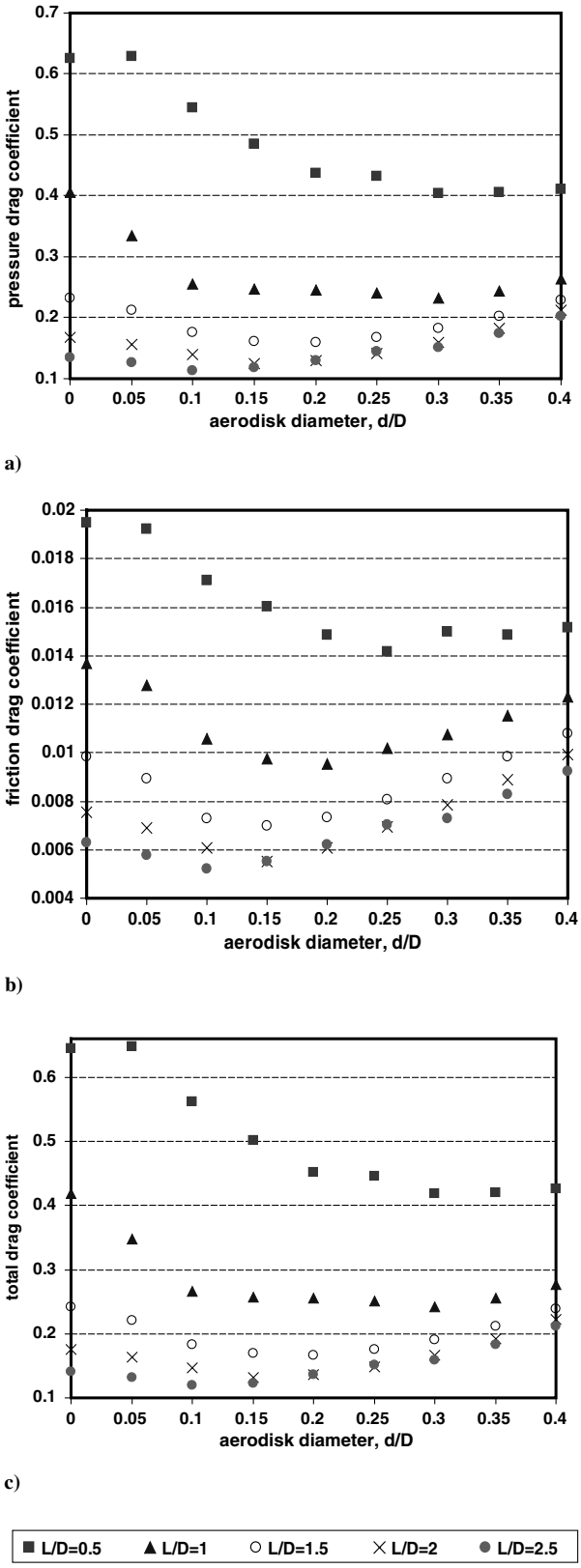

Fig. 36 Variation of drag coefficients with all models' designs: a) pressure, b) friction, and c) total.

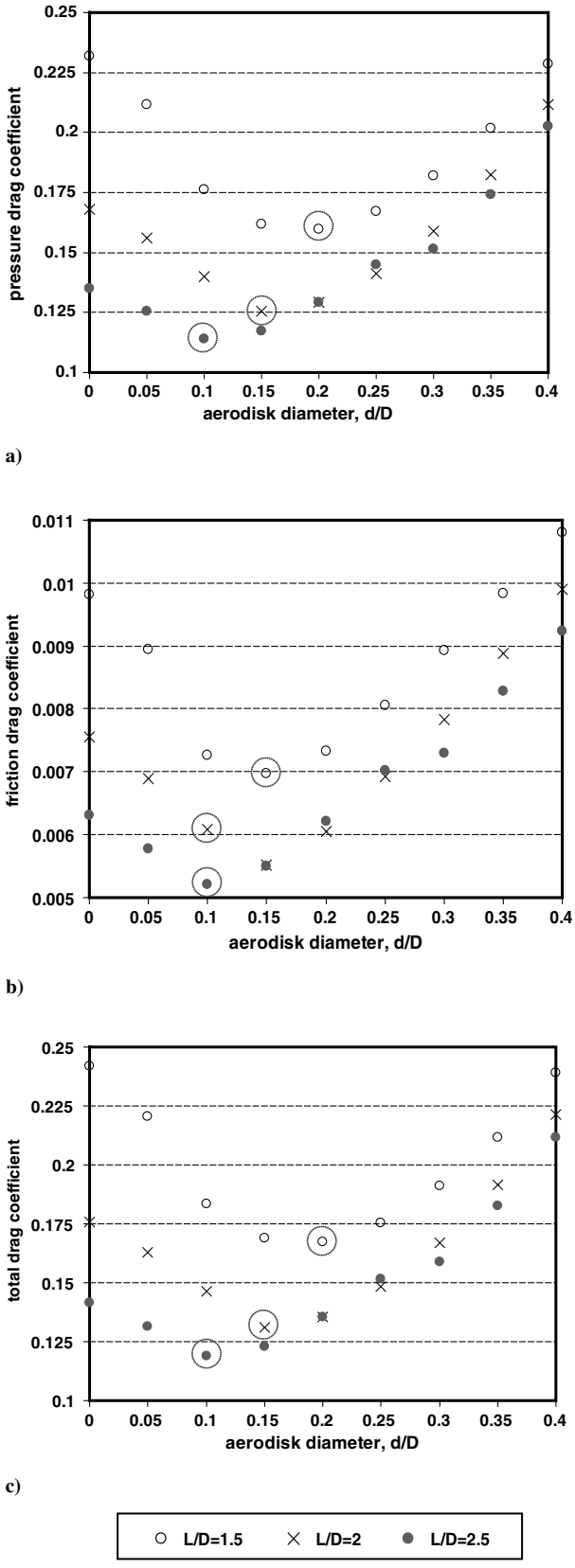

Fig. 37 Variation of drag coefficients with models' designs: a) pressure, b) friction, and c) total.

a model with a specific spike length, there exists an optimum size of the aerodisk that yields a minimum drag (marked by the dashed circles). Moreover, this optimum size decreases for longer spikes.

V. Conclusions

The high drag force experienced by blunt bodies in hypersonic flow can be significantly reduced by mounting a spike at the stagnation point of the blunt nose. Instead of using a pointed spike, mounting an aerodisk at the tip of the spike can provide further drag reduction. In the present work, a numerical investigation has been conducted on a hemispherical body equipped with a spike and a hemispherical aerodisk. The spike length and aerodisk diameter varied up to 2.5 and 0.4 of the body diameter, respectively. The mechanism of drag reduction was explained for both pointed spikes and aerodisks using a novel approach. In this approach, the dividing streamline of the shear layer was assumed to outline an effective body that replaces the original spiked blunt body. The shape of the effective body and the status of flow stability were found to be dependent on the energy level of the dividing streamline expressed by its total pressure. The superiority of the aerodisk in reducing the drag was explained as twofold: first, encouraging the separation of the dividing streamline and (in many cases) pushing the separation point radially away from the spike axis, thereby yielding a more slender effective body; and second, reducing the overall downstream pressure field by the action of expansion fan at the aerodisk shoulder.

For the models and flow conditions investigated here, a stable flow was evident for models with a spike longer than the model diameter. However, a larger aerodisk can stabilize the flowfield for models with shorter spikes. The drag reduction provided by the aerodisk was found to depend on both spike length and aerodisk size. For a specific spike length, there existed an optimum aerodisk size that would produce the minimum drag. This optimum size was found to be inversely proportional to the spike length.

References

[1] Menezes, V., Saravanan, S., Jagadeesh, G., and Reddy, K. P. J., "Experimental Investigations of Hypersonic Flow over Highly Blunted Cones with Aerospikes," *AIAA Journal*, Vol. 41, No. 10, 2003, pp. 1955–1966. doi:10.2514/2.1885

[2] Heubner, L. D., Mitchell, A. M., and Boudreaux, E. J., "Experimental Results on the Feasibility of an Aerospike for Hypersonic Missiles," AIAA Paper 95-0737, 1995.

[3] Kalimuthu, R., Mehta, R. C., and Rathakrishnan, E., "Experimental Investigation on Spiked Body in Hypersonic Flow," *The Aeronautical Journal*, Vol. 112, No. 1136, 2008, pp. 593–598.

[4] Mehta, R. C., "Flow Field Computations over Conical, Disc and Flat Spiked Body at Mach 6," AIAA Paper 2009-325, 2009.

[5] Holden, M., "Experimental Studies of Separated Flows at Hypersonic Speeds. Part I—Separated Flows over Axisymmetric Spiked Bodies," *AIAA Journal*, Vol. 4, No. 4, 1966, pp. 591–599. doi:10.2514/3.3494

[6] Wood, C. J., "Hypersonic Flow over Spiked Cones," *Journal of Fluid Mechanics*, Vol. 12, No. 4, 1962, pp. 614–627. doi:10.1017/S0022112062000427

[7] Calarese, W., and Hankey, W. L., "Modes of Shock Wave Oscillations on Spike Tipped Bodies," *AIAA Journal*, Vol. 23, No. 2, 1985, pp. 185–192. doi:10.2514/3.8893

[8] Kabelitz, H., "Zur Stabilität Geschlossener Grenzschichtablösegebeite an Konischen Drehkörpern bei Hyperschallströmung," DLR, FB 71-77, 1971.

[9] Alexander, S. R., "Results of Tests to Determine the Effect of a Conical Windshield on the Drag of a Bluff Body at Supersonic Speeds," NACA RM-L6K08a, 1947.

[10] Mair, W. A., "Experiments on Separation of Boundary Layers on Probes in front of Blunt-Nosed Bodies in a Supersonic Air Stream," *Philosophical Magazine*, Series 7, Vol. 43, No. 342, July 1952, pp. 695–716.

[11] Crawford, D. H., "Investigation of the Flow over a Spiked-Nose Hemisphere-Cylinder," NASA TN-D-118, Dec. 1959.

[12] Yamauchi, M., Fujii, K., and Higashino, F., "Numerical Investigation of Supersonic Flows Around a Spiked Blunt Body," *Journal of Spacecraft and Rockets*, Vol. 32, No. 1, 1995, pp. 32–42. doi:10.2514/3.26571

[13] Mehta, R. C., "Numerical Heat Transfer Study over Spiked Blunt Bodies at Mach 6.8," *Journal of Spacecraft and Rockets*, Vol. 37, No. 5, 2000, pp. 700–703. doi:10.2514/2.3622

[14] Mehta, R. C., "Numerical Analysis of Pressure Oscillations over Axisymmetric Spiked Blunt Bodies at Mach 6.8," *Shock Waves*, Vol. 11, No. 6, 2002, pp. 431–440. doi:10.1007/s001930200127

[15] Asif, M., Zahir, S., Kamran, N., and Khan, M. A., "Computational Investigations Aerodynamic Forces at Supersonic/Hypersonic Flow Past a Blunt Body with Various Forward Facing Spikes," AIAA Paper 2004-5189, 2004.

[16] Milicev, S. S., and Pavlovic, M. D., "Influence of Spike Shape at Supersonic Flow Past Blunt-Nosed Bodies: Experimental Study," *AIAA Journal*, Vol. 40, No. 5, 2002, pp. 1018–1020. doi:10.2514/2.1745

[17] Gnemmi, P., Srulijes, J., and Roussel, K., "Flowfield around Spike-Tipped Bodies for High Attack Angles at Mach 4.5," *Journal of Spacecraft and Rockets*, Vol. 40, No. 5, 2003, pp. 622–631. doi:10.2514/2.6910

[18] Kurbatskii, K. A., and Montanari, F., "Application of Pressure-Based Coupled Solver to the Problem of Hypersonic Missiles with Aerospikes," AIAA Paper 2007-462, 2007.

[19] Gauer, M., and Paull, A., "Numerical Investigation of a Spiked Blunt Nose Cone at Hypersonic Speeds," *Journal of Spacecraft and Rockets*, Vol. 45, No. 3, 2008, pp. 459–471. doi:10.2514/1.30590

[20] Maull, D. J., "Hypersonic Flow over Axially Symmetric Spiked Bodies," *Journal of Fluid Mechanics*, Vol. 8, Part 4, 1960, pp. 584–592. doi:10.1017/S0022112060000815

[21] Kenworthy, M., "A Study of Unsteady Axisymmetric Separation in High Speed Flows," Ph.D. Dissertation, Department of Aerospace and Ocean Engineering, Virginia Polytechnic Inst. and State Univ., Blacksburg, VA, 1978.

[22] Feszty, D., Badcock, K., and Richards, B., "Driving Mechanisms of High-Speed Unsteady Spiked Body Flows, Part 1: Pulsation Mode," *AIAA Journal*, Vol. 42, No. 1, 2004, pp. 95–106. doi:10.2514/1.9034

[23] Feszty, D., Badcock, K., and Richards, B., "Driving Mechanisms of High-Speed Unsteady Spiked Body Flows, Part 2: Oscillation Mode," *AIAA Journal*, Vol. 42, No. 1, 2004, pp. 107–113. doi:10.2514/1.9035

[24] Panaras, A. G., "Pulsating Flows About Symmetric Concave Bodies," *AIAA Journal*, Vol. 19, No. 6, 1981, pp. 804–806. doi:10.2514/3.7816

[25] "U. S. Standard Atmosphere, 1976," NASA TM-X-74335, 1976.

[26] Chapman, D. R., Kuehn, D. M., and Larson, H. K., "Investigation of Separated Flows in Supersonic and Subsonic Streams with Emphasis on the Effect of Transition," NACA TR 1356, 1957.

[27] "Equations, Tables, and Charts for Compressible Flow," Ames Aeronautical Lab., NACA TR 1135, 1953.

[28] Guenther, R. A., and Reding, J. P., "Fluctuating Pressure Environment of a Drag Reduction Spike," *Journal of Spacecraft and Rockets*, Vol. 14, No. 12, 1977, pp. 705–710. doi:10.2514/3.57253

G. Palmer
Associate Editor